Title
Microscale investigation of the corrosion performances of low-carbon and stainless steels in highly alkaline concretes

Author
Itty, Pierre-Adrien

Publication Date
2012

Peer reviewed|Thesis/dissertation

Microscale investigation of the corrosion performances of low-carbon and stainless steels in highly alkaline concretes

By

Pierre-Adrien Itty

A dissertation submitted in partial satisfaction of the

requirements of the degree of

Doctor of Philosophy

in

Engineering – Civil and Environmental Engineering

in the

Graduate Division

of the

University of California, Berkeley

Committee in charge:

Professor Paulo JM Monteiro, Chair
Professor Claudia Ostertag
Professor Hans-Rudolf Wenk

Fall 2012

Abstract

Microscale investigation of the corrosion performances of

low-carbon and stainless steels in highly alkaline concretes

by

Pierre-Adrien Itty

Doctor of Philosophy in Civil and Environmental Engineering

University of California, Berkeley

Professor Paulo JM Monteiro, Chair

Low-carbon steel shows good stability with respect to corrosion when embedded in ordinary portland cement concrete. This is due to the high alkaline content of the concrete pore solution favoring the formation of an iron oxide film that naturally keeps the steel in a passive state. With the rise of new types of concretes, based on different chemistries, the durability of reinforcements made out of low-carbon steel is at stake. Among the new concrete types, inorganic polymer concretes are characterized by an alkalinity of their pore solution at an early age that is higher than the one found in ordinary portland cement (OPC) concrete. The impact of these higher alkalinities on the stability of the passivity layer needs to be investigated. Low-carbon steel coupons are immersed for 2 days in four different solutions with hydroxide concentrations spanning from 0.1 mol/L to 3.7 mol/L. These solutions simulate the alkalinity of the pore solutions found in OPC concrete and three different types of inorganic polymer concretes. Stainless steels are often employed when the corrosion performances of low-carbon steel are insufficient. Whether duplex and ferritic stainless steels perform better in these environments, and thanks to which mechanism, is analyzed following the same procedure.

This work carries a multiscale approach of the corrosion performances of low-carbon and stainless steels in various highly alkaline environments. First, the few-nanometer-thick passive film is analyzed by combining traditional electrochemical tests with x-ray photoelectron spectroscopy (XPS). The corrosion performance of the passive films is measured by the polarization resistance method, and the stability of the iron oxides is evaluated by the cyclic potentiodynamic polarization method. XPS measures both the oxide composition of the film, and its thickness. Then, once the passive film breaks down, the corrosion of steel embedded in cement paste is studied at the micrometer scale, and the formation of corrosion products is monitored *in-situ* by micro-computed tomography (μCT). The acquisition of three-dimensional images is then crucial in understanding the mechanism of corrosion of steel in concrete.

Results show that when exposed to alkalinities higher than OPC pore solutions, the film growing on low-carbon steel (ASTM A36) is thinner and poorer in iron(III)-oxide. This goes in parallel with a decrease of the corrosion performances. Synchrotron-based XPS depth profiling show that the film formed after immersion in the 0.1 mol/L solution for 2 days is 4.1 nm-thick, with a 1.6 nm-thick inner-layer of Fe_3O_4, and an iron(III)-oxide outer-layer. On duplex stainless steel (UNS S32101), the iron oxide film grows thinner and poorer in iron(III)-oxide, but it gets enriched in chromium oxide – up to 4 times – as the alkalinity increases. This enrichment stabilizes the corrosion performances at higher alkalinities. The XPS depth profile shows that the film grown for 2 days in the 0.1 mol/L solution is 2.8nm-thick and contains chromium(III)-oxide in its outer-layer.

On a subsequent μCT study of steel embedded in cement paste, the passive film is broken down, and active corrosion induced by applying a galvanostatic anodic current of +5 mA/cm^2 to a steel electrode embedded in cement paste. Low-carbon steel (ASTM A36) is homogeneously etched away and a homogeneous layer of corrosion products forms at the interface steel/cement paste with a thickness of 40 μm after 3 hours. The induced pressure eventually fractures the cement paste cover, and corrosion products migrate out of the cracks. In the case of ferritic stainless steel (UNS S41000), the film depassivates locally, pits are formed, and concentrate the formation of corrosion products. Over 3 hours, 73 μm of corrosion products accumulates and their localized expansion creates more extensive damage on the cement paste cover.

While low-carbon steel shows considerably lower corrosion performances at higher alkalinities, stainless steels can postpone the onset of corrosion by forming a stronger passive film. However, local breakdown of the passive film formed on stainless steels can induce greater damages to the reinforced concrete structure once active corrosion starts.

To my parents,
Michèle and Jean-François

To my colleague and dear friend,
Marijana

To the newcomers,
Paul-Antoine and Victor

TABLE OF CONTENT

LIST OF FIGURES

LIST OF TABLES

Chapter 1: Introduction

In 2002, nearly 15% of the bridges in the United States were rated as structurally deficient with steel corrosion as the major cause (Federal Highway Administration 2002). Aggressive agents such as deicing chemicals, marine environment or atmospheric carbonation that commonly attack concrete, can often cause premature corrosion of its steel reinforcement (Mehta and Monteiro 2006). As corrosion products expand along the concrete-steel interface, the concrete may crack (Mehta and Gerwick Jr 1982), compromising the long-term performance of the structure. In ordinary portland cement concrete (OPC concrete), due to the high pH in its pore solution, a protective oxide layer—called the "passive film"— forms naturally on the steel reinforcement, thus preventing the early onset of corrosion (Montemor, Simoes, and Ferreira 1998). Although the corrosion performance of steel in OPC concrete has been the subject of numerous studies (Mehta and Gerwick Jr 1982; Montemor, Simoes, and Ferreira 1998; Mancio 2008; Freire et al. 2009; Sánchez et al. 2007; Ghods et al. 2011; Sánchez-Moreno et al. 2009; Andrade and González 1978), new kinds of studies are now investigating the natural growth of the passive film, and the kinetic of its layered structure (Sánchez-Moreno et al. 2009; Sánchez et al. 2007).

Furthermore, little is known about the corrosion behavior of the steel within inorganic polymer concretes (IPC, also known as geopolymer concretes), seen by some as a viable and more environmentally-friendly alternative replacement for OPC concrete (Habert, d' Espinose de Lacaillerie, and Roussel 2011; Deventer et al. 2010). These new concretes are characterized by highly alkaline pore solutions (pH higher than 14), and only a few studies have investigated how this may impact the corrosion behavior of their potential steel reinforcement (Miranda et al. 2005). This work aims to expand the knowledge base of such concretes, as well as regular OPC concretes, with the primary focus directed towards the initiation of corrosion in these types of concrete.

Finally, new types of economical stainless steels are investigated to improve the durability of structures subjected to aggressive corrosion environment. Of prime interest are low-nickel stainless steels; with lower amounts of nickel to reduce the costs, they have corrosion performances that meet the needs of the concrete industry (Bertolini et al. 1996; Callaghan 1993; García-Alonso et al. 2007; Criado et al. 2011; Bautista et al. 2009). This work aims to expand the knowledge base of such stainless steels, as well as low-carbon steel, with focuses directed towards the initiation and the propagation of corrosion.

1.1. Corrosion of steel in concrete

Corrosion is an electrochemical process: it involves electrical current (flow of charges in a conductor) and chemical reactions (loss and gain of electrons through oxidation and reduction reactions). Corrosion requires electrical currents: an ionic current path from the cathode to the anode, and an electronic path from the anode to the cathode. Corrosion requires chemical reactions at the anode and at the cathode, located at the

surface of the metal. At the cathode, oxygen reacts to reduce water. At the anode, iron is oxidized and produces electrons that are consumed at the cathode. When these four elements (ionic current path, electronic path, cathode, and anode) are brought together, a corrosion cell is formed and corrosion happens.

In reinforced concrete, the steel embedded in the concrete ensures the flow of electrons from the anode to the cathode. Hydrated cement paste is a porous material, whose pores are filled with an aqueous solution. This pore solution contains numerous dissolved ions (e.g. OH^-, Ca^{2+}, Na^{2+}, K^+… (Taylor 1997)), and acts as an ionic current path. Heterogeneities at the steel surface (such as grain structure and composition), but also heterogeneities in the electrolyte (such as local depletion of oxygen), determines if an area acts as a cathode or as a anode (Bentur, Diamond, and Berke 1997; Carino 1999). All requirements are met for corrosion in concrete to take place (Figure 1.1).

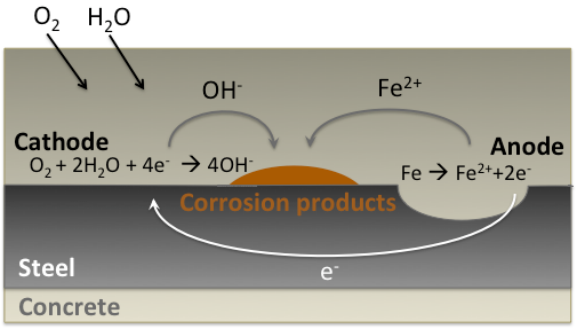

Figure 1.1 Corrosion cell forming on steel embedded in concrete

An oxidation reaction is a loss of electrons and an increase in oxidation state by a species. At the anode, iron is oxidized, producing electrons:

$$Fe \rightarrow Fe^{2+} + 2e^-$$

The electrons are transferred to the cathode via the conductive metal. A reduction is a gain of electrons and a decrease in oxidation state by a species. At the cathode, water is reduced, consuming electrons. In alkaline environments, the following reduction for water is possible:

$$2H_2O + 2e^- \rightarrow H_2 + 2OH^-$$

The mechanism of reduction of water can be diverse, depending on the concentration of dissolved oxygen in the electrolyte and the alkalinity of the solution. In the case of steel embedded in concrete, oxygen diffuses through the porous hydrated cement paste, and reaches the vicinity of the steel reinforcement. Therefore the following reduction reaction is more likely to happen:

$$O_2 + 2H_2O + 4e^- \rightarrow 4OH^-$$

These simple reactions are fundamental in the understanding of the corrosion of steel in concrete, but they do not grasp the actual complexity of the phenomenon. Iron can oxidize in different species, with different stabilities, and a better description of this process can be done by introducing the metal/solution interface potential difference.

1.1.1. Metal/solution interface potential difference

The most important parameter in corrosion is the interface potential difference, $\Delta\phi$. Across the interface between a metal M, and a solution S, there is a potential drop $\Delta\phi = \phi^M - \phi^S$, where ϕ^M is the metal electrical potential at the metal/solution interface, and ϕ^S is the solution electrical potential at the metal/solution interface (Bockris, Reddy, and Gamboa-Aldeco 2000). When a metal is inserted into solution, the charged particles in the solution do not experience the same set of coulombic forces at the interface with the metal than that in the bulk of the solution. The resulting electrical charge on the solution side of the interface creates an electric field that acts on the charged particles in the metal. In the metal, whereas the positively charged ion cores are stationery to a first approximation, the conduction electrons are very mobile. They move as to cancel the electric field inside the metal, and an electrical field arises at the interface between metal and the solution. This electrical field will exert a large effect on the movement of charged particle across the interface, as will occur for corrosion. At the equilibrium in a thermodynamic way, the metal/solution interface potential difference for the reaction $M^{++} + ne^- = M$, can be computed from the Nernst equation (Bockris, Reddy, and Gamboa-Aldeco 2000). By convention, the reaction is written as a reduction reaction. The equilibrium interface potential difference, $\Delta\phi_e$, is then:

$$\Delta\phi_e = \Delta\phi_e^0 - \frac{RT}{nF}\ln\frac{\Pi a_{reactant}}{\Pi a_{product}}$$

In this equation, $\Delta\phi_e^0$ is the standard reduction potential, R is the universal gas constant, T is the absolute temperature (in Kelvin), n is the number of electrons exchanged, F is the Faraday constant (96,500 C/mol), $\Pi a_{reactant}$ is the product of the activity of the reactants, and $\Pi a_{product}$ is the product of the activity of the products.

Note that only changes in interface potential differences can be measured, their absolute values are not accessible to measurement. Reference electrodes have non-polarizable interface, and can therefore overcome this problem. If the reference electrode is part of an electrochemical cell consisting of another metal electrode, then any changes in the cell voltage would not cause any change in the platinum/solution interface potential difference, it would just occur at the metal electrode interface. The most common reference electrode is the standard hydrogen electrode (SHE). It consists of a platinum wire immersed in an aqueous solution in which the activity of hydrogen is 1 (i.e., pH=0) and the pressure of hydrogen gas dissolved in the aqueous solution is 1 atmosphere (achieved by bubbling hydrogen through the solution). Platinum does not oxidize in this solution and is a very efficient catalyst for the hydrogen reduction and oxidation reactions.

Multiple reactions have to be considered to form all the different iron oxides. When these reduction-oxidation (redox) reactions are at equilibrium, it is possible to define a Nernst equation for the equilibrium potential $\Delta\phi_e$; when the products and the reactants are at the equilibrium, the potential is $\Delta\phi_e$. For potentials higher than $\Delta\phi_e$, the oxidation is thermodynamically possible. And for potentials smaller than $\Delta\phi_e$, the reduction is thermodynamically possible.

1.1.2. Pourbaix diagram

A Pourbaix diagram is an insightful way to represent electrochemical equilibria (Pourbaix 1974). On a Pourbaix diagram, boundaries are drawn on a potential versus pH graph in order to show the equilibrium possibilities. These boundaries define the stability regions for each of the iron oxides (Figure 1.2).

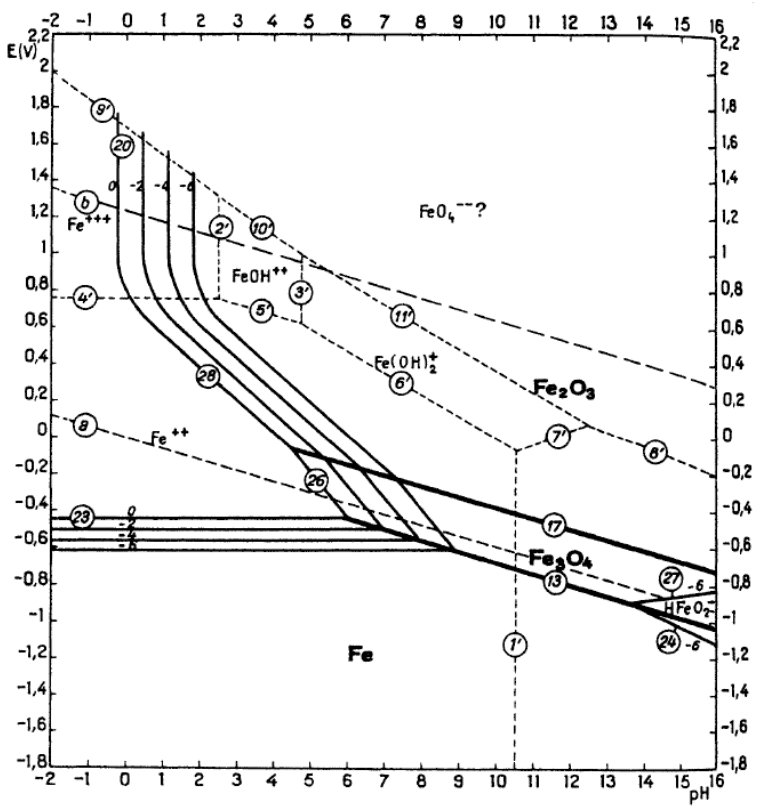

Figure 1.2 Pourbaix diagram for the system iron-water, at 25°C (considering as solid substances only Fe, Fe_3O_4 and Fe_2O_3, after (Pourbaix 1974))

When a redox reaction involves proton ions, H^+, it results in an oblique boundary in the Pourbaix diagram. An example is the oxidation of iron, Fe, into magnetite, Fe_3O_4, (label 13 in Figure 1.2). The equilibrium potential of the reaction $3Fe + 4H_2O \rightarrow Fe_3O_4 + 8H^+ + 8e^-$ is given by the Nernst equation, defined earlier:

$$\Delta\phi_e(Fe \rightarrow Fe_3O_4) = \Delta\phi_e^0 - \frac{RT}{8F}\ln\frac{[Fe]^3[H_2O]^4}{[Fe_3O_4][H^+]^8}$$

The terms in bracket are the activities of the species, with $pH = -\log[H^+]$, and with tabulated values from Pourbaix (Pourbaix 1974):

$$\Delta\phi_e(Fe \rightarrow Fe_3O_4) = -0.085 + 0.0591\ pH\ [V\ vs\ SHE]$$

The equation defining the line labeled 13 in Figure 1.2.

When a redox reaction does not involve proton ions, H^+, it results in a horizontal boundary (label 23 in Figure 1.2). As an example, the equilibrium of the reaction $Fe \rightarrow Fe^{2+} + 2e^-$ does not depend upon the pH (Pourbaix 1974):

$$\Delta\phi_e(Fe \rightarrow Fe^{2+}) = -0.440 + 0.0295 \log(Fe^{2+}) \; [V \; vs \; SHE]$$

Finally, for non-redox reactions, a vertical boundary is drawn on a Pourbaix diagram (label 1' in Figure 1.2). For example, the equilibrium for the reaction $Fe^{2+} + 2H_2O \rightarrow HFeO_2^- + 3H^+$ does not depend upon the potential (Pourbaix 1974):

$$pH_{eq}(Fe^{2+} \rightarrow HFeO_2^-) = 10.53$$

Some iron oxides are soluble (e.g. Fe^{2+}, $HFeO_2^-$, Fe^{3+}) and some others are insoluble (e.g. Fe_3O_4, Fe_2O_3). Once formed, insoluble iron oxides will remain deposited on the surface of the metal, and will not diffuse away. Note that at higher pH, there is a full region where insoluble iron oxides are formed (Fe_3O_4 and Fe_2O_3). This region is called the passivity region (Pourbaix 1974) because the insoluble iron oxides can form a protective layer that will hinder further corrosion: this layer is called the passive film, and is of main interest in concrete because of the high alkalinity expected in its pore solution.

Pourbaix diagrams are insightful in describing the equilibria of a metal/solution system but one should keep in mind that they are only representing the thermodynamical behavior of pure metal and aqueous solutions at standard conditions. They for example provide no information about the kinetic parameters of the corrosion reactions. Furthermore, for alloys and for non-ideal systems, thermodynamic conditions of corrosion differ from those described by Pourbaix diagrams (Thompson et al. 2000). A detailed characterization of the properties of the passive film forming on steel at high pH is therefore required.

1.2. Passive film forming on steel in alkaline environments

The passive film is a protective oxide layer that forms on the surface of a metal, thereby preventing further corrosion. It is only a few nanometers thick, but it plays an extremely important role in protecting the underlying metals. In the 1960s, Nagayama and Cohen (Nagayama and Cohen 1962) showed that passive films formed by polarizing iron in a neutral buffer solution consist of a double-layered oxide film with an inner Fe_3O_4 and an outer γ-Fe_2O_3 layer. Based on electrochemical measurements using galvanostatic cathodic polarization (Nagayama and Cohen 1962) or, more recently, light reflectance techniques (Büchler, Schmuki, and Böhni 1997), *in-situ* measurements of film thickness demonstrate that it ranges from 2 to 4 nm. The distribution of oxides across the film is critical to its overall stability. Surface Enhanced Raman Spectroscopy (SERS) has proven useful in monitoring the production of different oxides while the steel is polarized. For example, Mancio (Mancio 2008) and Schroeder (Schroeder and Devine 1999) identified an inner-layer containing Fe_3O_4 and an outer-layer containing iron(III)-oxide species with some maghemite (γ-Fe_2O_3). Previous works on iron in 0.1 M NaOH solutions indicates a gradual oxidation of the oxide film changing from magnetite Fe_3O_4 to hematite Fe_2O_3 with increasing potential (Joiret et al. 2002), which corresponds to a gradual decrease in the iron(II) oxide content in the passive as determined by XPS surface analyses (Haupt and Strehblow 1987).

There exist two main mechanisms of passive film breakdown: carbonation and chloride attack. Carbon dioxide (CO_2) can diffuse through the porous concrete and react with the sodium, potassium, and calcium cations present in solution; it results in big decrease in the pH of the pore solution (even below a value of pH 9) (Tuutti 1980). At lower pH, the passive film will lose its stability and break down. Carbonation will be maximal when the humidity is high enough for the aqueous reaction to happen and the air is dry enough for CO_2 to diffuse freely i.e., for relative humidity ranging from 40 to 80% (Rosenberg, Hansson, and Andrade 1989). Chloride ions can also diffuse through concrete and reach the steel reinforcement. The mechanism of chloride breakdown is not known with certainty (Hime 1993), but it is known that when the chloride to hydroxide ratio in the vicinity of the steel reaches a certain threshold, it causes a disruption of the passive film (Rosenberg, Hansson, and Andrade 1989). In the worst case both oxygen and chloride are allowed to reach the steel reinforcement; this is the case for splash zone in structures on coastal areas. Therefore, in marine environment, in hot and humid areas, or when the concrete cover is thin, an early onset of corrosion is expected, which reduces the service life of the structure.

1.3. Active corrosion of steel embedded in concrete

Corrosion processes can generally be divided into initiation and propagation period. Once the passive film breaks down, it ends the initiation period, and corrosion of the steel reinforcement is free to propagate in the concrete.

1.3.1. Observing corrosion in concrete

Carino reviews some of the nondestructive methods to assess the corrosion conditions in a reinforced concrete structure (Carino 1999). In the half-cell potential method, the voltage between the reinforcement and a copper-copper sulfate half cell is measured while the half cell is moved around on the surface to map the potential. High negative potential areas are indicating the areas with a high likelihood of having corrosion activity. Concrete resistivity can be measured by a four-electrode system. It is a direct measurement of the ease of migration of ions in concrete, and therefore a good estimate of the corrosion activity. Finally, a polarization resistance test measures the change in open circuit potential when a small external current is applied to the cell. The slope of the potential-current curve gives the polarization resistance, which is directly proportional to the corrosion rate.

Scanning Electron Microscopes (SEM) is the instrument of choice when studying the microstructure of concrete in general (Scrivener 2004) and corrosion propagation in concrete structures in particular (Caré et al. 2008). Magnification of SEM instruments can easily go up to 10,000X, it allows to observe features smaller than one μm. In backscattered detection (BSD) mode, denser elements are shown brighter than lighter elements, giving good contrast to distinguish iron oxides from steel and cement paste (Figure 1.3). Energy dispersive spectroscopy (EDS) maps can also probe the elemental composition of the surface of the sample. If SEM is providing important information about materials, there are also several drawbacks arising from sample preparation. To observe the surface, it is required to slice the sample, bring it to vacuum, and coat it with

a thin film of either gold or carbon to favor electron conduction. Cutting the sample may introduce stresses and cracks in the sample in addition to the one originating from corrosion for example (Figure 1.3). Furthermore, handling the freshly–cut surface in ambient air and then bringing it to vacuum may further oxidize and dehydrate the corrosion products. Sample preparation for SEM can significantly alter the surface of the sample. Furthermore, once the sample has been prepared it is not possible to monitor its evolution past this point, preventing the use of in-situ study, or simpler before/after comparison. Finally, once cut, only information at the surface of the sample is accessed, and no information about its 3D structure can be detected. Scrivener emphasized that carrying a SEM analysis of the microstructure of concrete overestimates the thicknesses of features, shifts the particle size distribution toward smaller particles, and loses the connectivity information of a pore network (Scrivener 2004).

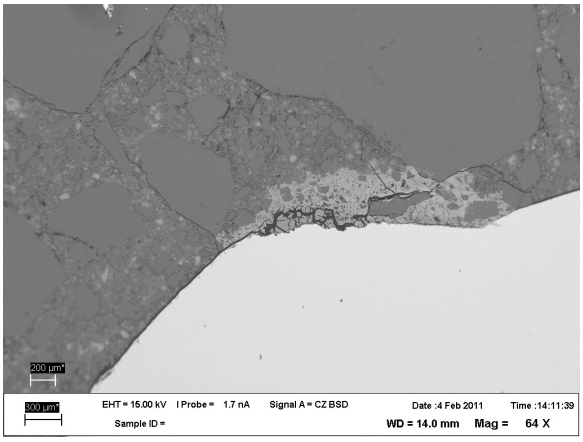

Figure 1.3 BSD SEM image of a corroded steel/cement paste interface at a 15 kV energy and a 1.7 nA probe current. In BSD, the cement paste is darker (top), corrosion products are lighter (middle), and steel is bright (bottom). The crack across the corrosion products zone has been introduced by sample preparation.

1.3.2. Corrosion propagation in concrete

During the propagation period, iron is reduced and reacts with oxygen and water to form iron oxide/hydroxides. The latter have larger specific volumes than metallic iron (Figure 1.4, (Patnaik 2003)), and as corrosion products are filling up the pores of the interfacial zone, radial pressure at the steel/concrete interface is generated. Once the pressure of corrosion products exceeds the tensile strength concrete will crack. Piltner and Monteiro investigated the stress and strain distribution in these composite phases by solving Mushkelishvili's problem for reinforced concrete structures (Piltner and Monteiro 2000). They were however not able to quantify the coefficient of expansion, p (the ratio between the specific volumes of rust and steel) for corroding steel reinforcement. Shodja *et al.* developed a numerical model based on the gradient reproducing kernel particle method (GRKPM) to compute the corrosion behavior of reinforced concrete (Shodja, Kiani, and Hashemian 2010).

Once cracks have developed and reached the surface of the concrete, corroding agents like seawater, deicing chemicals, or carbon dioxide will easily reach the steel reinforcement and more corrosion is expected. The cracking of the concrete cover has been studied by Andrade *et al.* (Andrade, Alonso, and Molina 1993). While impressing a current of 10 or 100µA/cm^2, they monitored the deformations at the surface of the concrete reinforced specimens. They started to observe cracks at the surface (width ~0.1 mm), when the reinforcement's section got only slightly reduced (~20-µm-thickness loss). The cracks also formed along the reinforcing bars, confirming that radial pressure induced transversal tension rupture of the concrete.

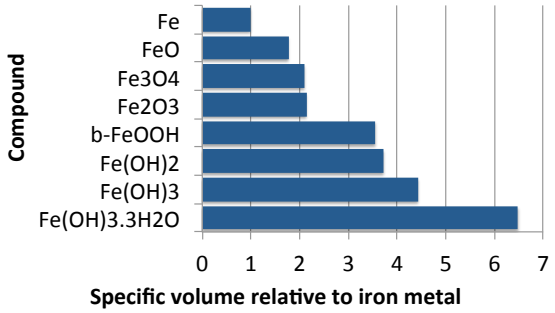

Figure 1.4 Specific volume relative to iron metal for common iron oxides/hydroxides (Patnaik 2003).

But the mechanism of crack propagation and widening in the concrete still remains incomplete. Zhao *et al.* sliced a corroded specimen (cyclic exposure to sea water for 2 years) in multiple 10 mm-thick sections (Zhao et al. 2012). Then, based on images from an optical microscope, they correlated crack width, volume of rust, to steel section loss. In another experimental set-up, Michel *et al.* studied corrosion in 2cm-thick mortar samples using the high penetration of hard x-rays for non-invasive investigation (Michel et al. 2011). Using x-ray attenuation measurements, they were able to observe the corrosion products building-up, inducing the initiation of cracks, and their further propagation in a time-resolved manner. They were however limited by the resolution of the x-ray camera (a pixel was 0.89mm x 0.89mm) and they lack information about the 3D structure of the cracks and the corrosion products.

1.3.3. Pitting corrosion

It is possible to compute the metal loss in an oxidation reaction ($A \rightarrow A^{n+} + n.e^{-}$). According to Faraday's equation, the mass, m, of oxidized metal is computed by

$$m = ItM/nF$$

where I is the current, t is the time, M is the metal molar mass, n is the number of exchanged electrons, and $F = 96{,}500\ C/mol$ is Faraday's constant.

The corrosion thickness loss, δ, is obtained by dividing m by the exposed surface of metal A, and by its density, ρ:

$$\delta = itM/nF\rho$$

where i is the current density. For iron, $n = 2$, $M = 55.9\ g/mol$, $\rho = 7.87\ g/cm^3$, hence

$$\delta = 1.332it\ [\mu m]$$

with i in mA/cm^2 and t in $hours$. Previous studies (Piltner and Monteiro 2000; Andrade, Alonso, and Molina 1993) reported an identical value of $0.0116 I_{corr} T\ [mm]$ with I_{corr} in $\mu A/cm^2$ and T in $years$.

Faraday's equation gives a good estimate of metal loss as a function of the corrosion current density. Nevertheless, reinforced concrete is a composite material, with multiple heterogeneities. Concentrations of chloride ions, and local weaknesses of the passive films are made possible. A small area of depassivated steel is a good candidate to form an anode, and, with the rest of the structure acting as a cathode, a corrosion cell is created. The difference in surface area between the anode and the cathode can generate high local corrosion rates. It is an example of a broader phenomenon called pitting corrosion.

As the potential of the metal is raised, aggressive anions such as chloride adsorb onto the surface of the film. At a given potential, the oxidation rate of the metal suddenly increases. If the metal surface is examined with the naked eye, it appears to be uncorroded. However, when observed with a microscope, small pits can be seen in the metal. These pits may penetrate deeply into the metal or severely undercut the surface. In either case, the size of the hole at the surface is underestimating the true extent of the corrosion damage. In addition, the solution inside the pit is stagnant and possesses a low pH and high chloride concentration. This aggressive solution chemistry prevents the formation of a protective, passive film on the surface of the metal in the pit and causes a high rate of active dissolution. The propagation of a pit is autocatalytic: once started, it grows at an ever-increasing rate.

The formation of pits weakens the steel reinforcement by reducing its cross-section, but, more important, it will localize the corrosion and therefore increase the stresses in some parts of the steel/concrete interface. González *et al.* measured the depth of pits by visual inspection of corrosion induced specimens (González et al. 1995). Analyzing a large variety of specimens and ways of inducing corrosion, they found that pits could be up to 16 times deeper than the average penetration calculated by weight loss or Faraday's equation.

1.4. Interest in using stainless steels as reinforcement in concrete

Most of the reinforced concrete structures are using low-carbon steel as reinforcement. In 2000, more than 7 million tons of steel was recycled from car bodies, appliances, and old reinforcing steel to make new reinforcing steel (Concrete Reinforcing Steel Institute 2008). This recycled material is cheap, and in the alkaline environment found in concrete, it shows good corrosion resistance thanks to the naturally forming passive film. However, steel-reinforced concrete can experience harsh environments that will cause premature corrosion and deterioration of the structure (Bentur, Diamond, and Berke 1997; Broomsfield 1997).

Numerous ways of fighting corrosion in reinforced concrete structures have been investigated and implemented:

(1) Corrosion resistant alloys (e.g. stainless steels) can replace low-carbon steel, their higher corrosion performances stopping, or, at least, slowing down corrosion (Bertolini et al. 1996).

(2) Coatings can also protect the steel reinforcing bars: epoxy powder coatings give an electrically and ionically impermeable layer over the steel (Manning 1996), or, in a process called galvanizing, zinc is deposited on the steel and corrodes more readily than concrete, providing a sacrificial protection.

(3) Admixtures, like chromates and nitrites, can inhibit corrosion of the steel (Berke and Weil 1992).

(4) The impermeability of concrete can be reduced by coating its surface.

(5) A potential can be impressed on steel in concrete to ensure it remains in the passive state. This process is called cathodic protection.

The most common of these options is to coat the reinforcing bar with epoxy (ACI Committee E-701 2006). However after several cases of early deterioration were observed on bridges in the Florida Keys in 1986, the influence of defects and low-bonding could give quite unpredictable corrosion performances for epoxy-coated reinforcing bars (Manning 1996). Conversely, the corrosion protection provided by stainless steel is not lowered by defects, and new stainless steels meeting required mechanical strengths at lower costs give new incentives in studying this option for combating corrosion in reinforced concrete structures.

1.4.1. Grades of stainless steels

Stainless steels exist in different types, depending on their chemical composition but also on the crystal structure that iron stabilizes into. The mechanical and chemical specifications for each type of stainless steel bar are summarized in the ASTM standard A276 (A276 2012). Austenitic stainless steels contain a minimum of 16% of chromium and enough nickel (around 8%) to stabilize iron in an austenitic crystalline phase. Ferritic stainless steels have better mechanical properties than austenitic stainless steels but have lower corrosion resistance, with nickel contents lower than 2.5% but chromium contents from 10.5% to 30%. In martensitic stainless steel, iron is stabilized in the martensite structure, forming steel that is stronger than austenitic or ferritic stainless steel. With chromium contents from 11.5% to 18% and little nickel, it also has lower resistance to

corrosion. Finally, duplex stainless steels contain both austenitic and ferritic crystal structures, combining high strength and high corrosion resistance; they have high chromium (from 21% to 27%) and high molybdenum contents (up to 5%) with lower amounts of nickel. Example compositions for ferritic, and duplex stainless steels (Top12, and LDX 2101 respectively) are given in Table 2.1.

Austenitic steels have shown very good corrosion performances but are expensive due to the high costs of nickel. There is therefore a strong incentive to find alternatives providing both adequate costs and corrosion resistance. Researchers are investigating the corrosion behavior of new types of stainless steels, where nickel has been replaced by manganese to reduce costs (García-Alonso et al. 2007; Elsener et al. 2011). García-Alonso *et al.* observed that, when embedded in chlorine-contaminated mortar and in concrete slabs for 2 years, the corrosion performances of these manganese-bearing steels are comparable to traditional 304 and 316 stainless steels (García-Alonso et al. 2007). Additionally, other studies proposed to use lower concentration of chromium and nickel (e.g. ferritic stainless steel) where the high cost / high corrosion resistance of austenitic stainless steel is not required (e.g. for structures subjected to mild marine environments) (Callaghan 1993).

1.4.2. Passive film forming on stainless steels

The good corrosion resistance of stainless steels comes from the presence of nickel and chromium as alloying elements. In contact with water, chromium oxidized into oxides that are more stable and more protective than iron oxides. In alkaline environments, the chromium oxide the most likely to form is chromium(III)-oxide Cr_2O_3. (see the Pourbaix diagram for the system chromium-water, Figure 1.5).

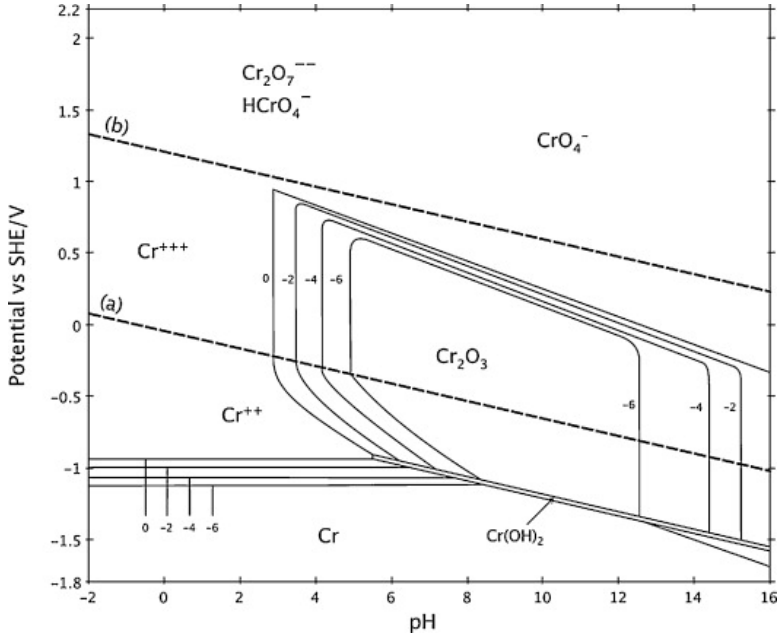

Figure 1.5 Pourbaix diagram for the system chromium-water, at 25°C. (Figure established considering anhydrous Cr_2O_3, after (Pourbaix 1974))

Artificially-grown passive films have been formed on austenitic and duplex stainless steels by cyclically polarizing the film 8 times. Electrochemical Impedance Spectroscopy (EIS) and XPS-depth profiling showed that molybdenum, while not present in the relatively thick film (about 100nm), favored the stabilization of chromium oxides, and enhanced the resistance of the passive film forming on duplex stainless steel (Abreu, Cristóbal, and Losada 2004). Potentiostatic studies of Fe/Cr alloys in alkaline environments showed an enrichment in chromium(III)-oxide in the films (Haupt and Strehblow 1989). XPS and micro-gravimetric study of the films suggested that the chromium oxide was present in the inner-part of the film formed on Fe-25Cr, and significantly slowed down the growth of the film (Schmutz and Landolt 1999).

Combined electrochemical and surface analysis of naturally grown passive films formed on various stainless steels confirmed a decrease of iron(II) with time, with a noticeable enrichment in chromium(III)-oxy-hydroxide with prolonged immersion time, and a nickel hydroxide enrichment was also observed on austenite stainless steels (Addari, Elsener, and Rossi 2008). Bertolini *et al.* studied the resistance to pitting corrosion by measuring the pitting potential for low-carbon, martensitic, austenitic and duplex stainless steels (Bertolini et al. 1996). In saturated calcium hydroxide solution, the stainless steels exhibited a critical chloride content for corrosion initiation of 0.5% for carbon steel, 2% for low chromium steels (Fe13Cr), and values superior to 5% for austenitic stainless steels.

Nickel-free manganese bearing stainless steels (type 204Cu, see Table 2.1) have been studied in alkaline (pH 12.6) and carbonated (pH 9) environments. A lower chromium enrichment of the passive films, and the formation of poorly corrosion resistant manganese oxides showed insufficient corrosion performances in comparison to traditional austenitic stainless steels (Bautista et al. 2009). Conversely, the resistance to pitting corrosion of nickel-free manganese bearing stainless steels is comparable to traditional austenitic stainless steels (Elsener et al. 2011).

1.5. Interest in inorganic polymer concretes

Ordinary portland cement concrete (OPC concrete) is the most used manmade material. In 2010, the yearly cement production was estimated at about 800 million tons (World Business Council for Sustainable Development 2009). The reasons for concrete's prevalent use are numerous: its flexibility and adaptability to different types of structures, its low maintenance requirements during the service life of the structures, and the widespread local availability of its constituents (Mehta and Monteiro 2006). However, the important demand and production of concrete have huge consequences on the environment, making the current concrete industry unsustainable (Mehta 2001). The mining for raw materials like limestone and clay can be detrimental for the environment, and the cement industry is also responsible for a significant part of the greenhouse gas emissions. On average, for each ton of portland cement clinker, 870 kilogram of carbon dioxide is released to the atmosphere (World Business Council for Sustainable Development 2009). As a consequence, OPC concrete production is responsible for 7% (2.1×10^9 tons) of the total anthropogenic carbon dioxide emissions (Mehta 2001). There

are strong incentives to investigate new alternatives that are more ecological but also with mechanical properties and ease of use comparable to OPC.

The significant improvements of inorganic polymer concretes (IPC), a subdivision of the alkali activated materials (Deventer et al. 2010), are creating greener opportunities in the field of structural and construction material. They mainly consist of alkali-activating an aluminosilicate source. The process of polymerization of an aluminosilicate source to form IPC (also know as geopolymers) has been described in a state of the art review by Duxson *et al.* (Duxson et al. 2007). The dissolution of a solid aluminosilicate source in highly concentrated aqueous alkaline solution produces aluminate and silicate species by alkaline hydrolysis. This dissolution of amorphous aluminosilicates is rapid at high pH, and also enhanced by increasing the temperature. Once dissolved, the aluminate and silicate species are incorporated into the aqueous phase, which in some case already contain silicate. In concentrated enough solutions this results in the formation of a gel, as the aluminate and silicate polymerize by condensation forming a gel. After gelation the system continues to rearrange and reorganize, it results in a three-dimensional aluminosilicate network commonly that is specific to inorganic polymer concretes. These different stages of structural reorganization determine the microstructure the material, which is critical in determining its physical properties. Relying on a different chemistry than OPC concretes, IPC show good acid and fire resistances, and high dimensional stability (Fernández-Jiménez, Palomo, and López-hombrados 2006). Furthermore, it shows fast mechanical strength development (Fernández-Jiménez and Palomo 2007).

Candidate source materials for IPC, rich in aluminosilicate, are widely available: from natural sources, such as natural pozzolans, to industrial by-products, like blast-furnace slags, fly ashes, *etc.* (Mehta and Monteiro 2006). Most natural pozzolans are derived from volcanic rocks and minerals. During volcanic activity, the magma, which is mainly composed of aluminosilicates, rapidly cools down and forms a porous glassy phase with high surface area, conferring it a good chemical reactivity in alkaline environments. Granulated blast furnace slags (GBFS) come from the production of iron in a blast furnace. When the liquid slag is quickly quenched in water, the lime, silica, and alumina remain in a glassy state. The water-quenched product is called granulated slag because of the sand aspect of its particles. Fly ash (FA) is a by-product of coal power plants. During the combustion of coal in thermal power plants, the volatile matter and carbon are burned while most of the mineral impurities such as clays, quartz, and feldspar melt at higher temperature. This fused matter is quickly transported to lower temperature where it solidifies as spherical particles of glass called FA. In addition to containing aluminosilicates, these waste materials present interesting cementitious and pozzolanic properties that found use as OPC replacement (up to 30%) in blended cements (Mehta and Monteiro 2006). For example, in France, the production GBFS is fully used by the cement industry and the use of FA in the cement industry is equal to 130% of its yearly production as there exist FA stock (Habert, d' Espinose de Lacaillerie, and Roussel 2011). However, in most parts of the world, a major part of these waste materials is still dumped in landfills, with negative impacts on the environment.

The possibility of using industrial waste materials in the production of inorganic polymer concretes eliminates a large portion of the CO_2 emissions associated with the

concrete production (Gartner 2004). But obstacles and problems are still along the way toward a broader use of IPC. Habert *et al.* pointed out that, even though the global warming impact of concrete can be reduced by the use of the inorganic polymer concretes, the production of the activation solutions (containing high concentrations of alkalis and silica) can have a detrimental impact on the environment (Habert, d' Espinose de Lacaillerie, and Roussel 2011).

In addition, the very high alkali content of IPC pore solutions can be a major issue in steel corrosion, possibly hindering its use in reinforced concrete structures. A recent study, for example, measured the content of sodium and potassium alkalis in the pore solution of some common IPCs (Lloyd, Provis, and Deventer 2010) (Table 2.2). Compared to the pore solutions associated with OPC concretes, IPC pore solutions typically have a pH between 12 and 13.8 and overall alkalinity in the 0.1 M - 0.6 M range. Remarkably, the overall alkalinity varied from 0.6 M to 3.7 M, depending on the raw materials used, and equivalent pH ranged from 13.8 to 14.6. When steel is embedded in concrete, it creates a very complex environment. The chemical composition of the pore fluid changes over time: diffusion of carbon dioxide, and chloride ions, can cause reduction of the alkalinity, and depassivation of the film, respectively. The material properties of the concrete cover are therefore also important for the corrosion performance, mainly due to the permeability with respect to the various corroding agents. This study does not address the latter issues. Synthetic solutions over a wide range of alkalinities were prepared to simulate the pore solutions found in OPC concrete as well as in IPC (Table 2.2).

1.6. Research scope

This work conducts research at both the nanometer and the micrometer scale. While x-ray photoelectron spectroscopy allows for probing characteristics of a few-nanometer thick oxide film, micro-computed tomography allows for imaging the corrosion products in cement paste samples with a diameter of about 5 millimeters and a resolution of few micrometers. The corrosion behaviors of different types of steels (low-carbon, ferritic, and duplex stainless steel) are compared at the microscale, and in environments with high alkalinities. The highlights of the research are given next:

1.6.1. Combined electrochemical and x-ray photoelectron spectroscopy characterization of the passive film at high alkalinities

A comprehensive understanding of the mechanism of growth of the passive film in environments with higher alkalinity remains incomplete. It has been reported that, in alkaline solutions, the passive film stability and the corrosion resistance continuously increases beyond pH 12 (Shalon and Raphael 1959). The stability of insoluble iron oxides is indeed highly dependent on the pH. However, after the work by Beverskog and Puigdomenech, the solubility of Fe_3O_4 is expected to increase with pH above pH 10 (Beverskog and Puigdomenech 1996). A similar trend is expected for iron(III)-oxides for pH higher than 8 (Cornell and Schwertmann 2003). Corrosion performances in the pH 12 – pH 13 range have been investigated (Ghods et al. 2009; Sánchez et al. 2007), but a thorough study of the corrosion resistance of passive film at alkalinities higher than pH

13.9 is still missing. Furthermore, stainless steels have shown to be the adequate solution to enhance the corrosion performances of reinforcement in marine environments (Callaghan 1993; Bertolini et al. 1996). But whether the addition of chromium in steel has a positive influence on the corrosion resistance at higher alkalinities remains unknown. This work concentrates on the properties of passive films forming on low-carbon and stainless steels in solutions from pH 13 to pH 14.6, which simulate the alkalinity found in the pore solutions of inorganic polymer concretes.

At the contact with concrete pore solution, steel naturally passivates since the alkalinity is high enough for stable iron oxides to form, as predicted by Pourbaix diagrams (Pourbaix 1974). Even so, most studies force the growth of the passive film by polarizing a steel electrode (Freire et al. 2009; Mancio 2008). Sánchez *et al.* used impedance spectroscopy to show that the characteristics of films grown naturally in simulated concrete pore solution differ from those produced polarized environments (Sánchez et al. 2007). In fact, to truly understand the mechanism of passive film formation, its growth should not be artificially induced. Other studies in simulated pore solution report that after few days of immersion the properties of the film were stabilized (Ghods et al. 2011; Sánchez-Moreno et al. 2009). This work focuses on the early stage of development just after immersion in solution and then chart the natural evolution of the film up to two days.

This work employs non-invasive XPS depth profiling to quantitatively resolve the layered structure and the thicknesses of the iron oxides present in passive films formed in highly alkaline environments. While most x-ray photoelectron spectrometers perform depth profiling by sputtering (Ghods et al. 2011), synchrotron-based XPS offers a non-invasive way to probe the depth of oxide films. In particular, the Ambient Pressure X-ray Photoelectron Spectroscopy (AP-XPS) endstation at beamline 9.3.2 of the Advanced Light Source at the Lawrence Berkeley Laboratories (Grass et al. 2010) provides information about composition, thickness, and oxidation states with a probing depth of few nanometers.

This work uses experimental and analytical techniques to precisely investigate the early natural formation and stability of the passive film that forms as a protective oxide layer on low-carbon steel in specific highly alkaline environments. After 30 minutes immersion in solution, the stability of the naturally growing film was studied by electrochemical techniques and its oxide composition inferred by X-ray Photoelectron Spectroscopy (XPS). These data were compared with the growth of the passive film after 6 hours and up to 2 days of immersion, and the corrosion performances were evaluated by measuring the corrosion current density in all environments. Finally differences in corrosion behavior are explained through XPS depth profiling and electrochemical cyclic potentiodynamic polarization of the steel.

1.6.2. Micro-computed tomography for in-situ monitoring of corrosion propagation of stainless steels

To better understand the corrosion propagation in concrete, it is important to get information about the type and volume of the iron oxides, the morphology of cracks forming in the paste, and their evolution with time. None of the traditional techniques (section 1.3) are ideal to investigate many of the aspects of corrosion in concrete, and in particular are not able to grasp its three dimensional morphology. Micro-computed tomography (μCT) can help getting over some of these obstacles. The high penetration of x-rays can image the samples without damaging them. It is a non-invasive tool, which allows monitoring the same sample at different times. Its advantages have already been presented while studying the evolution of the microstructure of hydrating cement paste (Gallucci et al. 2007). Along with images with resolution and contrast comparable with SEM, Gallucci *et al.* obtained a 3D representation of the pore network, and computed the cement paste's porosity and tortuosity at different hydration stages.

Most studies on crack formation relies on external observations (Andrade, Alonso, and Molina 1993) or on cutting open the samples after extensive corrosion (Zhao et al. 2012). These techniques hinder a full understanding of the mechanism of corrosion in concrete. This work proposes to obtain a true 3D representation of the corrosion products migration and the crack patterns in a time-resolved manner. Furthermore once the 3D structure of a corroded sample is obtained, it is possible to compare the results with crack initiation models developed by other researchers. μCT can help characterizing the pressure coefficient defined by Piltner and Monteiro (Piltner and Monteiro 2000), or refine the model proposed by Shodja *et al.* to include the penetration of corrosion products inside microcracks (Shodja, Kiani, and Hashemian 2010).

Of major interest is the formation of corrosion pits in chloride contaminated environments (González et al. 1995). μCT can follow the *in-situ* formation of corrosion pits; it provides additional insight about their formation kinetic. The development of pits on galvanostatically corroding stainless steel immersed in a 0.1M NaCl solution has already been successively studied using μCT by Ghahari *et al.* (Ghahari et al. 2011).

1.7. Organization of the chapters

The materials and the methods employed for this study are presented in chapter 2. Three grades of steel were tested in five different environments: they were embedded in cement paste, and also immersed in four solutions differing by their alkalinity. Three different techniques were employed: a potentiostat/galvanostat evaluated the corrosion performances of the steels, X-ray photoelectron spectroscopy (XPS) allowed the measuring the oxidation states of the passivation layer forming on steel, and micro-computed tomography (μCT) imaged in a non-destructive way the corrosion of the steel reinforcement embedded in cement paste.

The early growth of the passive film forming on low-carbon steel is studied in chapter 3. The low-carbon steel samples were immersed in solutions with high alkalinity simulating the pore environment found in inorganic polymer concretes. A combined electrochemical and XPS investigation evaluated the corrosion resistance of the passive film formed in these environments.

The passive film forming on LDX 2101 duplex stainless steel is studied in chapter 4, following the same methodology as for low-carbon steel in the previous chapter. The main difference is that synchrotron-based XPS was used to resolve the layering structure of the chromium-bearing passive film formed on LDX 2101 stainless steel.

The mechanisms of corrosion forming on low-carbon, Top12 ferritic, and LDX 2101 duplex stainless steels are investigated in chapter 5 using μCT. Galvanostatic anodic polarization allowed step-by-step corrosion of the reinforcement, while the morphology of the corrosion products and the induced cracks were non-destructively monitored by μCT.

The conclusions of this comprehensive study are drawn in chapter 6. Characteristics of the passive film at the nanometer-scale are linked with results on the corrosion products formation at the micrometer-scale. Finally, recommendations are given on the corrosion performances in concrete for the different grades of steel.

Chapter 2: Materials and methods

2.1. Materials

Steel samples were cut from reinforcing bars, and turned on a lathe to remove the ribs and produce a smooth 7.9-mm-diameter cylinder. Three grades steels were chosen: low-carbon, Top12, and LDX 2101. Their chemical compositions are given in Table 2.1.

Table 2.1 Chemical composition of investigated steels

Grades	ASTM or UNS	Chemical composition, % by weight								
		C	Cr	Ni	Mn	Mo	S	Si	Cu	N
Low-carbon	A36	≤0.26	-	-	-	-	≤0.05	-	-	-
Top12	S41000	≤0.03	10.5/12.5	0.3 - 1.0	≤1.50	-	≤0.015	≤1.00	-	≤0.030
LDX 2101	S32101	0.04	21.0/22.0	1.35/1.70	4.0/6.0	0.1/0.8	≤0.015	≤1.00	-	0.2/0.25

2.2. Investigation of the passive film properties

The passive film properties of low-carbon and LDX 2101 duplex stainless steels were investigated after immersion in four simulated pore solutions. They were prepared by dissolving analytical grade sodium hydroxide (98.9%) and potassium hydroxide (86.5%) in distilled water in order to simulate the alkalinity in the pores of different types of concretes (Table 2.2).

Table 2.2 Composition of the solutions simulating the alkalinity found in concretes

Solution	[Na] (M)	[K] (M)	Equivalent pH	Simulated pore solution from:
0.1 M	100	0	13	OPC concrete
0.6 M	0.612	0.003	13.8	Fly ash type F IPC[a]
1.6 M	1.567	0.015	14.2	Fly ash type C IPC[a]
3.7 M	3.617	0.077	14.6	Ground granulated blast-furnace slag IPC[a]

[a] Alkalinity of pore solutions extracted from 7-day-old inorganic polymer cement (IPC) samples from Lloyd *et al.* (Lloyd, Provis, and Deventer 2010). Ca, Al, Fe concentrations (<1 mM), and Si concentrations (<10 mM) were measured to be negligible in comparison to Na and K content.

2.2.1. Electrochemical measurements of the passive film properties

For the electrochemical measurements of the passive film properties, the steel rods were embedded in epoxy, leaving a 0.49-cm^2 disk in contact with the solution. Prior to each measurement, the electrode was polished with a 1200-grit silicon carbide sandpaper, degreased in acetone, and then rinsed in ethanol. They were then electrically connected to a GAMRY PCI4/750 potentiostat/galvanostat before immersion in 150 mL of solution. All potentials were measured with respect to a Saturated Calomel Electrode (SCE), using a graphite rod as counter-electrode. The solutions were saturated with respect to oxygen.

Since the passive film grows naturally in highly alkaline environments, the corrosion potential of the steel electrode, E_{corr}, was measured continuously after immersing the electrode in solution, providing indications on the stage of corrosion. The polarization resistance, R_P, was evaluated by polarizing the electrode from 10 mV below the corrosion potential to 10 mV above the corrosion potential at a scan rate of 0.167 mV/s. The slope of the potential, E, versus current density, i, at the corrosion potential gave the polarization resistance, $R_p = \Delta E/\Delta i|_{E=E_{corr}}$. Polarizing the electrode ± 75 mV around the corrosion potential provided β_c and β_a, the cathodic and anodic Tafel slopes, respectively, and the corrosion current density, i_{corr}, was computed through $i_{corr} = \beta_a\beta_c/(2.303(\beta_a + \beta_c)R_P)$. Cyclic potentiodynamic polarization of the electrodes was carried from -1300 mV to +500 mV at a scan rate of 2 mV/s, measuring the current density to get information on the thermodynamical behavior of the steel in each solution. Galvanostatic corrosion of steel was performed by imposing a constant current density, i_G, and measuring the potential of the electrode, E_G, with respect to the reference electrode.

2.2.2. XPS measurements of the passive film properties

For the XPS measurements of the passive film properties, coupons 1-mm thick were cut from the steel rod, polished to 600 grit on a mechanical mill for an hour on each side, and then hand polished for an additional five minutes using a 1200-grit sandpaper prior to degreasing in acetone and ethanol to provide an extremely smooth substrate for the passive film development. After immersion in the solution, the samples were mounted on the XPS sample holder in a box filled with Argon, and placed in the load lock chamber before being brought to the XPS chamber at ultra-high vacuum, about 10^{-9} Torr (Figure 2.1).

XPS measurements were performed at the AP-XPS endstation, beamline 9.3.2 of the Advanced Light Source (ALS) of the Lawrence Berkeley National Laboratory (Grass et al. 2010). While aluminum and magnesium atoms Kα lines are typical photon sources for XPS, with photon energies of 1486.7 eV and 1253 eV, respectively, at the AP-XPS endstation, the photon energy can be tuned from 250 eV to 850 eV to provide the optimal cross section for each species. Previous passive film studies (Jin and Atrens 1987; Ghods et al. 2009) used the Fe 2p peak, but synchrotron radiation at beamline 9.3.2 is optimized for the Fe 3p peak. The AP-XPS endstation can also collect XPS spectra at an elevated pressure up to several torrs, where experiments can be carried out in-situ. In this study,

however, only experiments under ultra-high vacuum conditions were performed. Fine scans of the Fe 3p peak (52.9 eV) and of the Cr 3p peak (42.1 eV) were measured at a photon energy of 500 eV, averaging over six sweeps at 0.1 eV/step. The software CasaXPS (Fairley) was used to subtract a Shirley background and deconvolve the different peaks. Binding energies were calibrated to the Fermi level. Furthermore, unique depth profiling abilities are available at the AP-XPS endstation. By tuning the incident photon energy in the 250-850 eV range, information at the surface is accessed without alteration or destruction, providing reliable quantitative data about both composition and thickness at the nanometer scale: increasing the incident photon energy causes an increase in the kinetic energy of photoelectrons from a given core level, and, thus, varies the probing depth for specific chemical species. As an example, the probing depth of XPS for γ-Fe_2O_3 is approximately 1.5 nm at a photon energy of 250 eV, while at 850 eV it increases to 3.9 nm; these lengths are ideal to study few-nanometer-thick oxide layers. The incident photon energy was increased by increments of 250 eV from 250 eV to 850 eV.

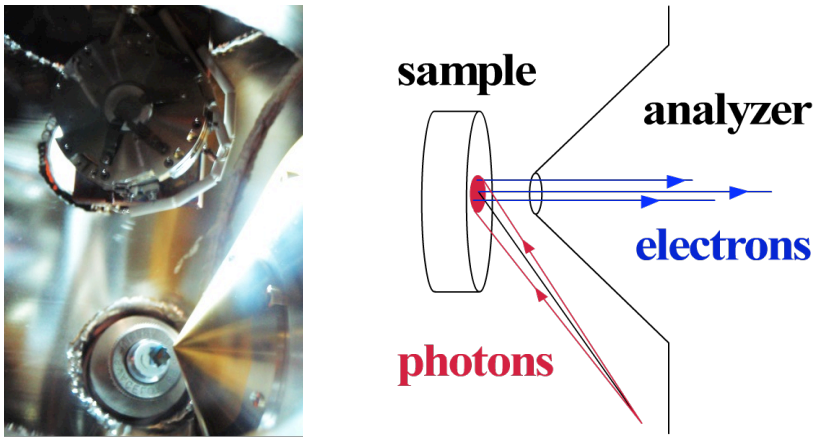

Figure 2.1 (a) X-ray photoelectron spectroscopy (XPS) experimental chamber: sample holder with steel sample (top center) away from the analyzer (bottom right), and x-ray beamline (bottom center), (b) schematic of the generation of photoelectrons

2.3. Investigation of the corrosion propagation

For the active corrosion study, the rebars were thinned out on a lathe and polished to create a cylinder with a diameter smaller than 0.5 mm and a length of about 5 mm. An isolated electrical wire was then connected to them to ensure electrical connection. Connection between the steel and the wire was covered with impermeable paint, to minimize the risk of corrosion of wire or galvanic corrosion between the two. The specimens were placed into cylindrical molds with 5 mm in diameter, and cement paste was poured into them (Figure 2.2).

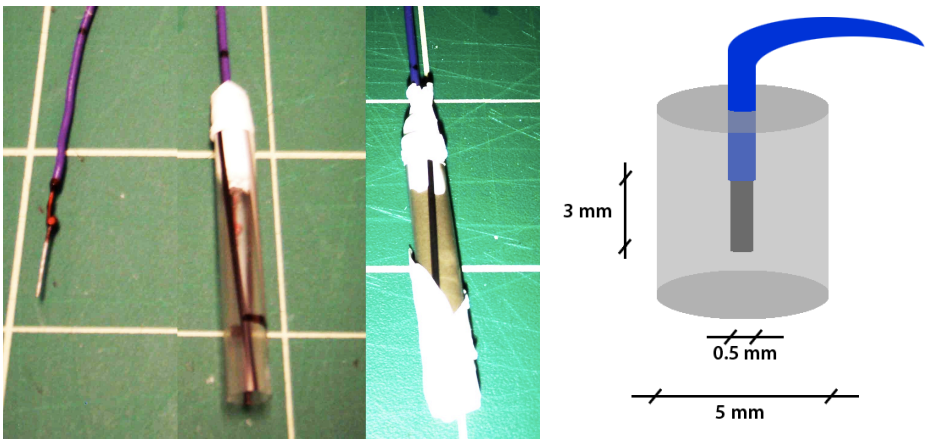

(a) **(b)**

Figure 2.2 (a) Preparation of samples for micro-computed tomography. From left to right: thinned rebar soldered to an electrical wire, rebar and wire centered in the mold, mold filled with cement paste and wrapped in Teflon® tape. (b) Schematic with the average dimensions of the sample.

The cement paste was obtained by mixing water with ordinary Portland cement type II at water to cement ratio of 0.45. The specimens were cured in a humidity chamber, with controlled humidity (95% RH) and temperature (20±2°C) for 1 day, demolded and additionally cured in humidity chamber for the rest of the experiment. For the exact dimensions of the samples, see Table 2.3.

Table 2.3 micro-computed tomography specimens' dimensions

	Steel reinforcing bar			Cement paste matrix	
	Diameter (mm)	**Exposed length (mm)**	**Exposed surface area (cm^2)**	**Diameter (mm)**	**Height (cm)**
Low-carbon	0.46	3.5	0.051	5	22
Top12	0.37	3.56	0.04	5	25
LDX 2101	0.50	3.25	0.052	5	23

2.3.1. Electrochemical measurements of the state corrosion

For the measurements of active corrosion, the samples were placed in a solution containing 3.5% per mass of sodium chloride to support the electron transfer. The end of the electrical wires was then electrically connected to a GAMRY PCI4/750 potentiostat/galvanostat. All potentials were measured with respect to a Saturated Calomel Electrode (SCE), while a stainless steel mesh surrounding the samples worked as a counter-electrode.

2.3.2. Micro-computed investigation of corrosion propagation

A micro-computed tomography (μCT) set-up consists of a radiograph while the sample is placed on a rotating stage. Projection x-ray images of the sample are taken upon parallel beam illumination and after each small increments of rotation of the sample stage. Using the Fourier slice theorem, the 3D structure of the sample is reconstructed based on the information from the projections. This method is called filtered back projection (Kak and Slaney 1999). At beamline 8.3.2 of the Advanced Light Source at the Lawrence Berkeley National Laboratory, synchrotron radiation is providing the photon source, thereby insuring a high flux of photons. The instrument covers a wide range of photon energy, from 10 to 45keV, allowing to optimize transmission for concrete samples from 1mm to a little more than 1cm. A set of optical lenses in front of the CCD detector also allows visualizing from a resolution of 3.3μm with a 2X lens (field of view is 8mm) to 0.65μm with a 10X lens (a field of view is about 2mm).

Micro-computed tomography (μCT) experiments were conducted at beamline 8.3.2 of the Advanced Light Source, Berkeley. A tomography set-up primarily consists of a radiograph instrument; Beer's law gives the X-ray intensity going through a sample of thickness *t*:

$$I = I_0\, exp(-\mu t)$$

where I is the X-rays intensity on the detector, I_0 is the initial intensity, and μ is the material's linear attenuation coefficient. The attenuated value for each pixel, $P(x', z)$, is then determined by:

$$P(x', z) = -\ln\left(I(x', z)/I_0\right)$$

Radiographic images are taken while the sample is rotated by small increments of the rotation angle, φ. The attenuated value, P, for each pixel (x', z) on the detector is the radon transform of the linear attenuation field, $\mu(x, y, z)$:

$$P(\varphi, x', z) = \iint_{\Omega} \mu(x, y, z)\delta(xcos\varphi + ysin\varphi - x')dxdy$$

The linear attenuation field, $\mu(x, y, z)$, gives a 3D representation of the sample. Using Fourier slice theorem (Kak and Slaney 1999), $\mu(x, y, z)$ was obtained for all x, y, and z by inverting the expression for $P(\varphi, x', z)$. This process is called reconstruction and the software Octopus was used on this purpose (Vlassenbroeck et al. 2010). The resolution of the reconstructed field, $\mu(x, y, z)$, therefore depends on the resolution of the image field, $P(\varphi, x', z)$, and adequate sampling of φ, x', and z is required.

For an adequate representation of the morphology of the samples a pixel size of 3.3μm (square pixels) was chosen, and a 2X lens was placed in front of the x-ray camera detector at beamline 8.3.2. The field of view was 8mm in width and 2mm in height. This provided the sampling for x' and z from the previous equation: x' varied from 0 to 8mm by 3.3μm increments, and z varied from 0 to 2mm by 3.3μm increments. Continuous tomography was performed, ie 1024 images were acquired while the stage was continuously rotating from 0 to +180°. This provided the sampling for φ in the previous equation: φ varied from 0 to +180° by increments of 0.18°. Samples were henceforth

represented with a voxel size of 3.3µm x 3.3µm x 3.3µm. A voxel is the 3D equivalent of a pixel.

At beamline 8.3.2, the X-ray camera detector is optimal for a transmission of 20% through the sample. It is possible to estimate the transmission through the sample, using Beer's law for two materials (steel and cement paste) in the path of the x-ray beam:

$$T = I/I_O = T_{steel}T_{cement} = \exp(-\mu_{steel}t_{steel})\exp(-\mu_{cement}t_{cement})$$

where T is the transmission, μ is the linear attenuation coefficient, and t is the thickness for the steel, and for the cement paste.

Table 2.4 Predicted attenuation through the samples

Photon energy	Linear attenuation coefficient (mm^{-1})		Transmission (%)	
	Steel	Cement paste	1mm steel 10mm cement paste	0.5mm steel 5mm cement paste
30 keV	6.46	0.25	0%	1%
40 keV	2.87	0.13	2%	12%
50 keV	1.55	0.09	9%	30%

The linear attenuation coefficient μ is a function of the energy of the incident x-rays (or photon energy). The photon energy at beamline 8.3.2 ranges from 10 keV to 45 keV. Therefore we investigated several scenarios, for different photon energies and different thicknesses of the samples (Table 2.4). A sample with a 1 mm-thick piece of steel was not giving satisfactory transmission (<20%) at any of the photon energies. Conversely, for a 0.5mm piece of steel embedded in 5 mm of cement paste, transmission near 20% was predicted in the 40-50 keV range. After experimentation at the tomographic microscope, a photon energy of 43 keV was decided as optimal for samples containing 0.5 mm of steel and 5 mm cement paste. This constrained the size of the samples. Another consequence was the exposure time: it took 350 ms in average to get enough photon counts on the detector and prevent saturation.

Viewing and analysis of the tomography datasets were conducted with the 3D visualization software Avizo® from VSG.

Chapter 3: Early age and growth of the passive film formed on low-carbon steel in highly alkaline environments

Low-carbon steel is the most widely used material for reinforcement in concrete structures (Concrete Reinforcing Steel Institute 2008). While it has been thoroughly studied in ordinary portland cement (OPC) concrete, its corrosion performances in new types of concretes have not yet been fully investigated. More specifically, inorganic polymer concretes (IPC) rely on a different chemistry than OPC concrete, and the alkalinity of their pore solution is expected to be higher (Lloyd, Provis, and Deventer 2010). This chapter investigates the properties of the passive film formed on low-carbon steel (composition in Table 2.1) in solutions simulating the alkalinity found in 4 different types of IPC (composition in Table 2.2). First, a combined electrochemical and x-ray photoelectron spectroscopy (XPS) analysis is carried at the early age of the passive film (the first 30 minutes). Then, the formation and growth of the passive film for up to 2 days is investigated using synchrotron-based XPS depth profiling. Finally the protective character of the passive film at higher alkalinities is put in parallel with the stability of its different iron oxides using cyclic potentiodynamic polarization measurements.

3.1. Early age of the passive film: the first thirty minutes

After immersion in the 0.1 M, 0.6 M, 1.6 M, and 3.7 M solutions, the corrosion potential of the low-carbon steel electrode increased rapidly for the first few minutes until it reached an arrest point, after which its increase slowed (Figure 3.1.a). This first stage of rapid increase occurred more rapidly with increasing alkalinity of the solution.

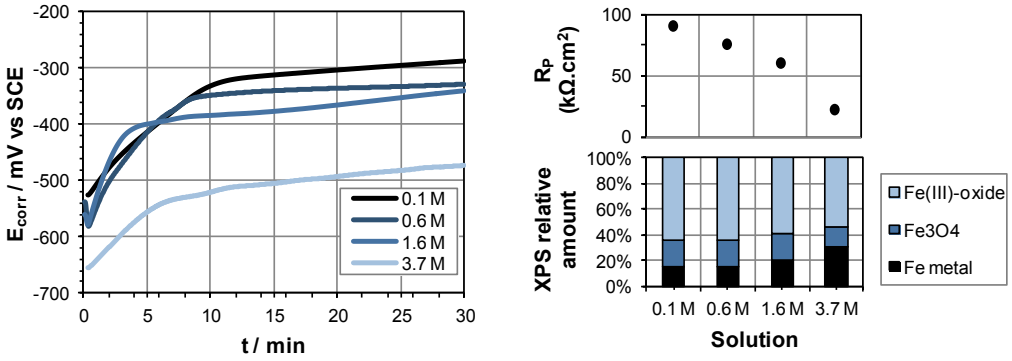

(a) **(b)**

Figure 3.1 Naturally grown passive films after immersion in 0.1 M, 0.6 M, 1.6 M, and 3.7 M solutions for 30 minutes. (a) Open circuit potential E_{corr}, (b, top) polarization resistance R_p, after 30 minutes of immersion (b, bottom) oxide relative amounts from XPS. See Table 2.2 for the compositions of the solutions.

After 30 minutes of immersion, the polarization resistance (Figure 3.1.b) was the highest for the 0.1 M solution, with 91 kΩ.cm^2, reaching 22 kΩ.cm^2 for the 3.7 M solution. The polarization resistance of the intermediate solutions fell between these values. To evaluate the polarization resistance, the steel was polarized -/+10 mV around the open circuit potential, E_{corr} (Figure 3.2.a). The (i,E)-curve crosses the axis $i = 0$ at $E = E_{corr}$, and its slope gives the polarization resistance, $R_P = \Delta E/\Delta i|_{E_{corr}}$. For low-carbon steel immersed in the 0.1 M solution, E_{corr}=-286 mV vs SCE and the resistance is R_P = 91 kΩ.cm^2.

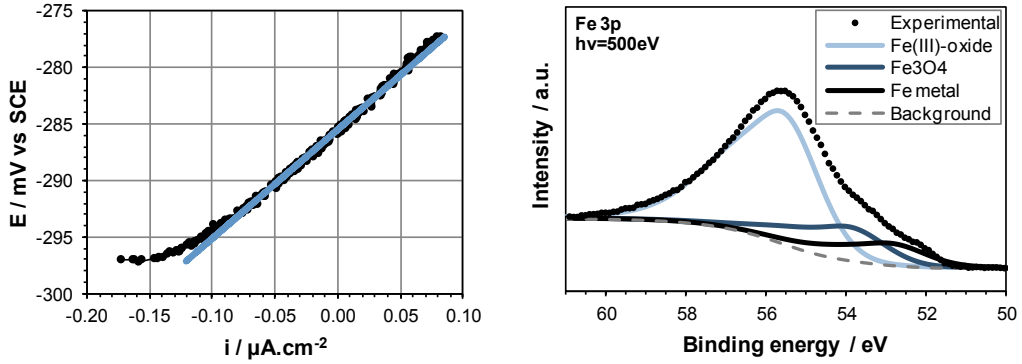

(a) **(b)**

Figure 3.2 Examples of data processing for the electrochemical and the XPS data. Low-carbon steel immersed for 30 min in the 0.1 M solution. (a) Polarization resistance measurement with linear regression around the open circuit potential. (b) Deconvolution of a XPS Fe 3p spectrum at 500 eV incident photon energy.

The oxide composition of the 30-minute old films was then determined from XPS Fe 3p spectra for the low-carbon steel coupons immersed for 30 minutes in the 0.1 M, 0.6 M, 1.6 M, and 3.7 M solutions. Based on results obtained from previous studies (Freire et al. 2009; Jin and Atrens 1987; Descostes et al. 2000; Brion 1980), the three peaks in Figure 3.2.b were identified as the following iron species: iron metal (oxidation state 0), magnetite (Fe_3O_4), and Fe(III)-oxides (e.g. γ-Fe_2O_3). The Fe 3p fitting line shape was chosen to be asymmetric Gaussian-Lorentzian with same full width at half maximum for all 3 peaks. We set the peak positions to be free in the fitting procedure, and a statistical analysis for the entire specimen set yielded consistent binding energies (BE) of 52.9 eV for iron metal, 53.9 eV for Fe_3O_4, and 55.6 eV for the Fe(III)-oxides, which is consistent with results by from previous studies (Descostes et al. 2000; Brion 1980). After 30-minute immersion, the samples showed substantial differences in the intensity of their iron metal peak, but a rather constant ratio between Fe_3O_4 and Fe(III)-oxide (Figure 3.1.b).

The presence of the iron metal peak indicated that the probing depth of XPS at 500 eV, about 3 nm, was larger than the thickness of the oxide layer: photoelectrons from the steel underneath the passive film could be detected, and the relative amount of the oxides over the metal is an indication of the oxide layer thickness. Strohmeier proposed a

method to evaluate the thickness of a uniform oxide layer (Strohmeier 1990), based on the intensity ratio between the oxides and the metal.

The thickness d_{ox} of the oxide film is computed by

$$d_{ox} = \lambda_{ox} ln[(N_m \lambda_m / N_{ox} \lambda_{ox})(I_{ox}/I_m) + 1]$$

where $\lambda_{ox} = 1.02$ nm is the inelastic mean free path (IMFP) of the oxide layer (assumed to be uniformly composed of Fe_2O_3), $\lambda_{ox}/\lambda_m = 1.1$ is the ratio between the oxide and the metal IMFP; $N_{ox}/N_m = 0.47$ is the ratio of the atomic densities of the oxides and the metal; and I_{ox}/I_m is the XPS peak area ratio between the oxides and the metal. The layer thicknesses ranged from 2.5 nm for the 0.1 M solution to 1.7 nm for the 3.7 M solution.

The ratio between Fe_3O_4 and Fe(III)-oxide did not vary significantly with the alkalinity of the solution. The proportion of Fe_3O_4 in the oxide content was 25% for the 0.1 M solution, and it decreased to 22% for the 3.7 M solution. Since Fe_3O_4 was more likely to form underneath the Fe(III)-oxides, its measured XPS contribution was less detectable, and thus its importance was underestimated in the oxide content of the films; they were richer in Fe_3O_4 than they appeared in the XPS results.

3.2. Growth of the passive film: from thirty minutes to two days

Passive films did not reach their full thickness in 30 minutes, and in the next stage of the study we investigated longer immersion to assess the stability of the films in the highly alkaline solutions. When immersed in the 0.1 M, 0.6 M, 1.6 M, and 3.7 M solutions for 2 days similar trends were observed for all solutions: the corrosion potential, E_{corr}, steadily increased for one day before stabilizing around a constant potential that is lower for specimens immersed in solution with higher alkalinity. The protective character of a passive film can be evaluated by measuring its corrosion current density: the lower the measured current, the more protective the film. We measured the corrosion current density, i_{corr}, after 30 minutes, 6 hours, and 2 days immersion for the 0.1 M, 0.6 M, 1.6 M, and 3.7 M solutions (Figure 3.3).

The corrosion current density was 0.504 $\mu A/cm^2$ after 30 minutes, and 0.119 $\mu A/cm^2$ after 6 hours for the 0.1 M solution. After 2 days this dropped to only 0.008 $\mu A/cm^2$. We observed similar decreases for the other solutions, except for an unexpected drop in corrosion current density in the 3.7 M solution between 30 minutes and 6 hours. XPS study of the passive films grown for 2 days in the 0.1 M and 3.7 M solutions yielded the iron oxide amounts on each film. The proportion of Fe_3O_4 in the oxide content was 7% for the 0.1 M solution, and 9% in the 3.7 M solution. Passive film thicknesses computed from Strohmeier equation gave 4.1nm for the 0.1 M solution and 3.0nm for the 3.7 M solution.

To examine the composition of the film over time, non-invasive XPS depth profiling was performed on a sample immersed in the 0.1 M solution. The contributions of iron metal (Fe^0), Fe_3O_4, and Fe(III)-oxides were measured for different photon energies (Figure 3.3.a). The relative concentration in iron metal (BE 52.9 eV) increased with increasing photon energy, whereby a homogeneous oxide layer formed over the steel. The relative intensity of the Fe(III)-oxide peak (BE 55.6 eV) decreased with the

photon energy, while the relative intensity of the Fe_3O_4 peak (BE 53.9 eV) increased. This indicated that the film contained more Fe(III)-oxide in its outermost layer, and that Fe_3O_4 was present in the innermost layer. The computations that follow quantify the development and stability of these layers.

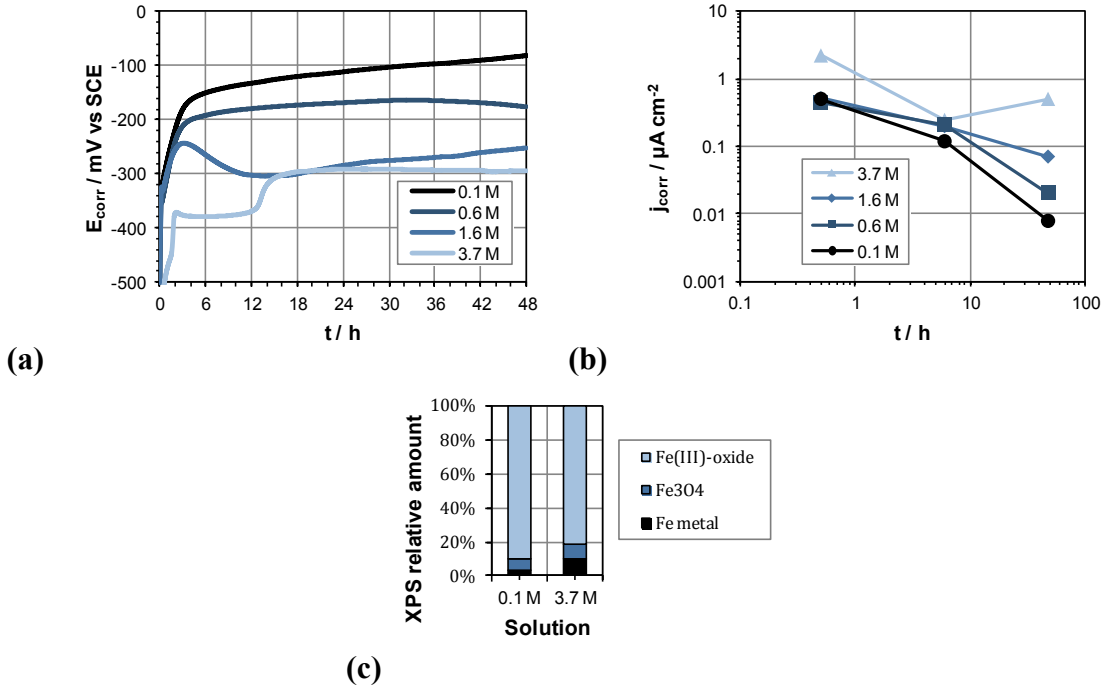

Figure 3.3 Naturally grown passive films after immersion in 0.1 M, 0.6 M, 1.6 M, and 3.7 M solutions from 30 minutes to 2 days. (a) Corrosion potential E_{corr} and (b) corrosion current density i_{corr} after 30 minutes, 6 hours, and 2 days (log-log plot). (c) Oxide relative amounts from XPS after 2 days.

The attenuation of an electron going through matter with a thickness t is $I/I_0 = exp(-t/\lambda)$ where I/I_0 is the attenuation, and λ is the electron IMFP, obtained from the predictive formulae by Gries (Gries 1996). The qualitative analysis suggested a homogeneous double layer formed on iron metal (subscript m) with an Fe_3O_4-rich innermost layer (subscript IL) and an Fe(III)-oxide-rich outermost layer (subscript IL).

With the three unknowns I_0, d_{IL}, and d_{OL} (the overall intensity, and the thicknesses of the inner- and outer-layers, respectively), the computed intensities are as follows:

$$\begin{cases} I_{OL} = I_0 N_{OL} \int_0^{d_{OL}} exp\left(-x/\lambda_{OL}\right) dx \\ I_{IL} = I_0 N_{IL} exp\left(-d_{OL}/\lambda_{OL}\right) \int_0^{d_{IL}} exp\left(-x/\lambda_{IL}\right) dx \\ I_m = I_0 N_m exp\left(-d_{OL}/\lambda_{OL}\right) exp\left(-d_{IL}/\lambda_{IL}\right) \int_{-\infty}^{0} exp\left(-x/\lambda_m\right) dx \end{cases}$$

where I is the peak area, N the volume density of Fe atoms, and λ the IMFP. The thicknesses are:

$$\begin{cases} d_{IL} = \lambda_{IL} ln\left[N_m\lambda_m/N_{IL}\lambda_{IL}\ I_{IL}/I_m + 1\right] \\ d_{OL} = \lambda_{OL} ln\left[\left(1 - exp\left(-d_{IL}/\lambda_{IL}\right)\right) N_{IL}\lambda_{IL}/N_{OL}\lambda_{OL}\ I_{OL}/I_{IL} + 1\right] \end{cases}$$

If the computed thicknesses were homogeneous in the range 350 to 650 eV for the samples immersed for 6 hours and 2 days, small discrepancies between the model and the sample immersed for 30 minutes may indicate roughness in the layered structure at the early stage of the passive formation.

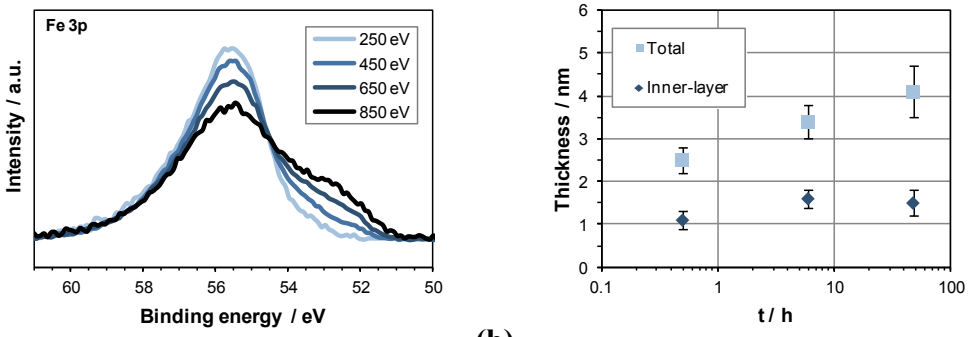

(a) **(b)**

Figure 3.4 Natural growth of the passive film in the 0.1 M solution. (a) XPS Fe 3p spectra with incident photon energies from 250 eV to 850 eV, and (b) thickness of the Fe_3O_4 inner-layer and total thickness of the Fe_3O_4 / Fe(III)-oxide layers after 30 min, 6 hours, and 2 days from XPS depth profiling.

Between 30 minutes and 2 days, the film thickened—from 2.5-nm to 4.1-nm thick (**Figure 3.4**.b). Furthermore, while the thickness of the Fe(III)-oxide outer-layer grew with time, the thickness of the Fe_3O_4 inner-layer stabilized around 1.5 nm after 6 hours.

3.3. Cyclic potentiodynamic polarization

Polarization of steel gives insight about the thermodynamic behavior and the stability of the iron oxides to develop in each solution (Freire et al. 2009; MacDonald and Roberts 1978). Through starting the cyclic potentiodynamic polarization at -1300 mV versus SCE, we measured an intense negative current for the 0.1 M, 0.6 M, 1.6 M, and 3.7 M solutions (**Figure 3.5**).

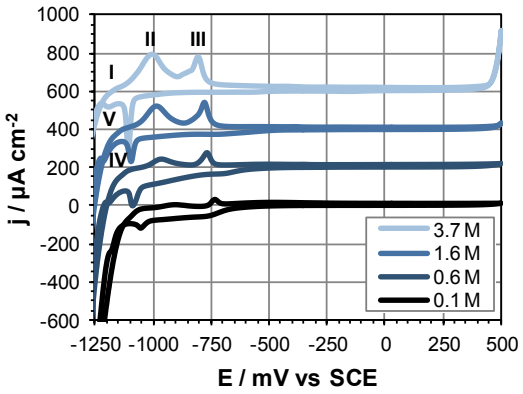

Figure 3.5 Cyclic voltammograms for low-carbon steel at a sweep-rate of 2 mV/s when immersed in the 0.1 M, 0.6 M, 1.6 M, and 3.7 M solutions. Results are offset by +200 µA/cm^2 increments. See Table 2.2 for the compositions of the solutions. On the anodic scan, they showed three oxidation peaks - labeled I, II, and III. On the cathodic scan, after a zero current density region, they showed two reduction peaks - labeled IV and V.

All oxide species present on the electrodes were reduced, as well as hydrogen for potentials lower than $E_0 = -244 - 59pH\ [mV\ vs\ SCE]$ (Pourbaix 1974). With increasing potential, the current density during the anodic scan first increased. Then, a shoulder occurred (labeled I, Figure 3.5), followed by two prominent peaks (labeled II and III, Figure 3.5) indicating that oxidations of iron into iron oxides took place. Above a given potential, and up to +500 mV, the steel entered the passive state; the current density stabilized around a small but greater than zero current density. However for the 3.7 M solution at just below +500 mV the potential reached the potential of electrolysis of water, and the current density rose significantly. On the cathodic scan, starting from +500 mV vs SCE, the current density was first zero: the passive film formed during the anodic scan protected the steel. Then, at lower potentials, two prominent peaks (labeled IV and V, Figure 3.5) indicated the reduction of the oxides formed during the anodic scan. In previous experiments, using SERS on low-carbon steel in a pH 13.85 solution, Mancio (Mancio 2008) identified species similar to $Fe(OH)_2$ at low potentials during the anodic scan, an increase in magnetite Fe_3O_4 coinciding with the third oxidation peak, and the presence of maghemite γ-Fe_2O_3 among other Fe(III)-oxide species for higher potentials. Using these results, peaks I and II were then assigned to the formation of Fe(II)-oxides species, peak III to the formation of Fe_3O_4**,** and the current density plateau to the

formation of Fe(III)-oxides. If the peaks labeled from I to V were present for the 4 solutions, then their positions and relative areas changed with increasing alkalinity. The peak positions decreased linearly with pH following the prediction by the work by Pourbaix (Pourbaix 1974). The magnitude of all peaks increased with increasing alkalinity. In particular, the relative importance of the oxidation peak II, associated with the formation of Fe(II)-oxide species, increased relative to the other peaks.

3.4. Discussion

After 30 minutes of immersion, the polarization resistance of the passive film formed in the 0.1 M, 0.6 M, 1.6 M, and 3.7 M solutions decreased with increasing alkalinity of the solution (Figure 3.1.b.). This indicated that the low-carbon steel passive film was less protective at higher alkalinities. XPS analysis of the Fe 3p peak showed that the film formed after 30 minutes was thinner in the 1.6 M and the 3.7 M solutions than in the 0.1 M and 0.6 M solutions (Figure 3.1.b.). This indicates that these films were thinner and, thus, less protective.

Next, during the following 2 days of immersion, the corrosion potentials increased, the current densities decreased, and the passive film grew stronger for all solutions (Figure 3.3). The non-invasive XPS depth profiling on a sample immersed in the 0.1 M solution showed that the film thickened with time, from 2.5 nm after 30 minutes to 4.1 nm after 2 days (Figure 3.4.b.). These thicknesses were similar to results obtained through ion sputtering by Ghods et al. (Ghods et al. 2011). In addition, the XPS depth profiling work showed that an Fe(III)-oxide outer-layer grew on top of a Fe_3O_4 inner-layer. This agreed with the cyclic potentiodynamic polarization measurements: Fe_3O_4 was stable at lower potentials and Fe(III)-oxides at higher potentials. From the low corrosion potential where Fe_3O_4 was likely to form, the corrosion potential increased, with Fe(III)-oxides growing on top of the Fe_3O_4 layer. At the same time, while Fe_3O_4 was produced at the metal interface, it could also oxidize into Fe(III)-oxide. Furthermore, the film became richer in Fe(III)-oxide with time, in agreement with the reaction model proposed by Sánchez et al. (Sánchez-Moreno et al. 2009). Additionally, the thickness of the Fe(III)-oxide layer was measured to grow from 1.4 nm at 30 minutes to 2.6 nm at 2 days.

Similar thickening behavior is expected for the samples immersed in the 0.6 M, 1.6 M, and 3.7 M solutions. Nevertheless, the decrease of the corrosion current density with time was less significant for solutions with higher alkalinity, so that the corrosion performance between samples immersed in the 0.1 M and the 3.7 M solution increased the difference to almost two orders of magnitude (Figure 3.3). This may arise from variable stability of iron oxides in alkaline environments. Beverskog et al. (Beverskog and Puigdomenech 1996) demonstrated that $Fe(OH)_2$ is not stable in highly alkaline media and, instead, soluble ions such as dihypoferrite $HFeO_2^-$ may form. From the cyclic votammograms (**Figure 3.5**), we obtained further information about the stability of the different iron oxides. On the anodic scan at oxidation peak II, dihypoferrite was likely to be produced, and the reaction is thermodynamically possible for potentials higher than $E_0\left(Fe \rightarrow HFeO_2^-\right) = 249 - 89pH + 30\log(HFeO_2^-)\ [mV\ vs\ SCE]$ (Pourbaix 1974).

During this process, some $Fe(OH)_2$ may deposit on the surface, in decreasing amounts with increasing pH ($\log(HFeO_2^-) = -18.30 + pH$ (Pourbaix 1974)). The relative intensity of the oxidation peak II grew more significantly with increasing alkalinity, suggesting that more Fe(II)-oxides were produced. Using sweep-reversal method on iron in a 0.1 M solution, MacDonald et al. (MacDonald and Roberts 1978) showed the oxides formed during oxidation peak II is reduced in reduction peak V. In this study, the ratio between oxidation peak II and oxidation peak V significantly increased, indicating that a large fraction of the oxidized species were not reduced, and likely went to solution as soluble products. Thus, our experiment confirmed Beverskog's results: more soluble iron oxides such as dihypoferrite formed at higher alkalinity. If the solubility of the Fe(II)-oxides was higher, then the oxide early stage sublayer formed during the early age and the subsequent passive film were less stable and probably had more defects.

3.5. Summary

The resistance of the passive film forming on low-carbon steel increases with time, and stabilizes after to 2 days. This resistance is accompanied by the thickening of the passive film layer, and its enrichment in iron(III)-oxide. X-ray photoelectron spectroscopy non-invasive depth profiling measured the film to be 4.1-nm thick, with a 1.6-nm Fe_3O_4 inner-layer and a 2.5-nm iron(III)-oxide outer-layer after a 2-day immersion in a solution with pH 13.

For solutions with higher alkalinities, from 0.6 mol/L to 3.7 mol/L, iron(II)-oxides are more soluble, hindering the formation of a strong passive film. There is a decrease in both thickness and Fe_3O_4 content of the passive film formed on low-carbon steel in these solutions. These are correlated with poorer corrosion performances for increasing alkalinities: the corrosion resistance decreases with alkalinity, and the resistance gain rate also decreases. After a 2-day immersion, the current density of the solution with 3.7 mol/L hydroxide becomes 50 times higher than for the solution with 0.1 mol/L.

For inorganic polymer concrete (IPC), the alkalinity is expected to span from 0.6 mol/L to 3.7 mol/L. In these environments, it has been demonstrated that low-carbon steel behaves poorly with respect to corrosion. If it is the case, other types of steels, such as stainless steels, should be studied in order to provide alternatives for building reinforced IPC structures resistant to corrosion.

In this study, the values for the alkalinity were taken after extracting the pore solution of 7-day-old IPCs (Lloyd, Provis, and Deventer 2010). Further studies should measure the alkalinity evolution in the pores of IPC samples older than 7 days. Indeed, IPCs are expected to carbonate faster than ordinary portland cement concretes because they do not contain calcium hydroxide to act as a buffer and keep the alkalinity higher than pH 12.6. Upon carbonation, the alkalinity of the pore solution can decrease as low as pH 9. This alkalinity evolution should therefor be integrated in the passive film growth environment to observe the time-dependence on its properties.

Chapter 4: Early age and growth of the passive film formed on duplex stainless steel in highly alkaline environments

The passive film formed on low-carbon steel has been seen to become thinner, less protective, and poorer in iron(III)-oxide with increasing alkalinity (Chapter 3). Other studies have shown that in harsh environments, stainless steels develop stronger passive films thanks to an enrichment in chromium oxide of their passive film (Addari, Elsener, and Rossi 2008; Bertolini et al. 1996). This chapter investigates the importance of the 21% of chromium present in LDX 2101 duplex stainless steel (Table 2.1) in solutions with alkalinities from 0.1M to 3.7M (Table 2.2). A combined electrochemical and x-ray photoelectron spectroscopy analysis of the passive film is first conducted at its early age (up to 30 minutes), and after 2 days. Then the thermodynamic stability of the oxides is assessed by cyclic potentiodynamic polarization. Finally, different layering models for the iron/chromium oxide film are proposed and compared to XPS depth profiling results.

4.1. Early age and growth of the passive film: from the first thirty minutes to two days

After immersion of the LDX 2101 duplex stainless steel sample in the 0.1 M, 0.6 M, 1.6 M, and 3.7 M solutions (Table 2.2), we measured the corrosion potential, E_{corr}, for 30 minutes. The value of E_{corr} increased rapidly for the first few minutes and then slowed down. The duration of these few minutes of rapid evolution got shorter with increasing alkalinity of the solution. After 30 minutes, the polarization resistance (Figure 4.1.a) was fairly constant for all four solutions with the highest resistance at 92 kΩ.cm^2 for the 0.1 M solution, and the lowest at 69 kΩ.cm^2 for the 1.6 M solution.

The oxide composition of the 30-minute old films was determined using the XPS Fe 3p and Cr 3p spectra for the LDX 2101 stainless steel samples immersed for 30 minutes in the 0.1 M, 0.6 M, 1.6 M, and 3.7 M solutions (Figure 4.1.a). No significant amount of nickel was detected in the film. To properly compare the XPS relative amounts of the two species, the intensity of the peaks were corrected to take into account the photoionization cross-section of iron and chromium. The area of XPS peak A, I_A, is related to the concentration of the species A, C_A, by the relationship: $I_A = FS\lambda\sigma_A C_A$, where σ is the cross-section of the sub-layer irradiated by the x-ray beams, F is the x-ray flux, λ is the mean free path of electrons, and S is a function of the apparatus. Therefore the relative amount of species A with respect to species B is: $C_A/C_B = I_A\sigma_B/I_B\sigma_A$. The photoionization cross-section for iron, and chromium are 0.25Mb, and 0.2Mb respectively (Yeh and Lindau 1985).

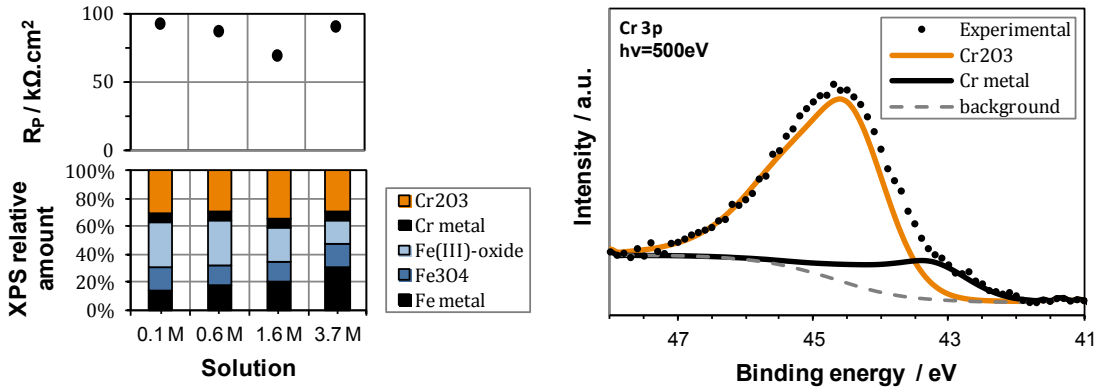

(a) **(b)**

Figure 4.1 Naturally grown passive films after immersion in 0.1 M, 0.6 M, 1.6 M, and 3.7 M solutions for 30 minutes. (a, top) polarization resistance R_p, (a, bottom) oxide relative amounts from XPS. See Table 2.2 for the compositions of the solutions. (b) Deconvolution of a typical XPS Cr 3p spectrum at 500 eV incident photon energy.

The analysis of the XPS Fe 3p peak followed the same procedure as described in Chapter 3, section 1. After 30 minutes, the iron composition in the films formed on the LDX 2101 stainless steel noticeably changed with the alkalinity of the solution (Figure 4.1.a). The contribution of the iron metal (Fe0) peak relative to the iron oxides peaks increased significantly with increasing alkalinity. The ratio between Fe_3O_4 and iron(III)-oxide remained constant at around 1/3 in the 0.1 M, 0.6 M, and 1.6 M solutions, and rose to 1/2 in the 3.7 M solution.

Based on previous studies (Shuttleworth 1980; Allen, Tucker, and Wild 1978), the two peaks in the XPS Cr 3p spectrum (Figure 4.1.b) were identified as chromium metal (oxidation state 0), and chromium(III)-oxide (Cr_2O_3). The Cr 3p fitting line shape was chosen to be asymmetric Gaussian-Lorentzian with same full width at half maximum for the two peaks. The peak positions were set to be free in the fitting procedure, and a statistical analysis for the entire specimen set yielded binding energies (BE) of 41.9 eV for chromium metal, and 43.6 eV for Cr_2O_3, which were consistent with results from previous studies (Allen, Tucker, and Wild 1978; Shuttleworth 1980). The intensities of the chromium metal and the Cr_2O_3 peaks were constant throughout the all set of solutions. Chromium metal contributed to 24% of the total metal contribution, which is in good agreement with the elemental composition (21-22%, Table 2.1). The chromium oxide (Cr_2O_3) represented 43% of the total oxide content, which is almost double of the metal relative contribution. This indicated enrichment of the oxide layer in chromium oxide.

Similar to low-carbon steel in Chapter 3, passive films formed on LDX 2101 stainless steel did not stabilize after 30 minutes. Longer immersions were investigated to assess the stability of the films in the highly alkaline solutions. When immersed in the 0.1 M, 0.6 M, 1.6 M, and 3.7 M solutions for 2 days similar trends were observed for all solutions: E_{corr} continued to steadily increase (Figure 4.2.a).

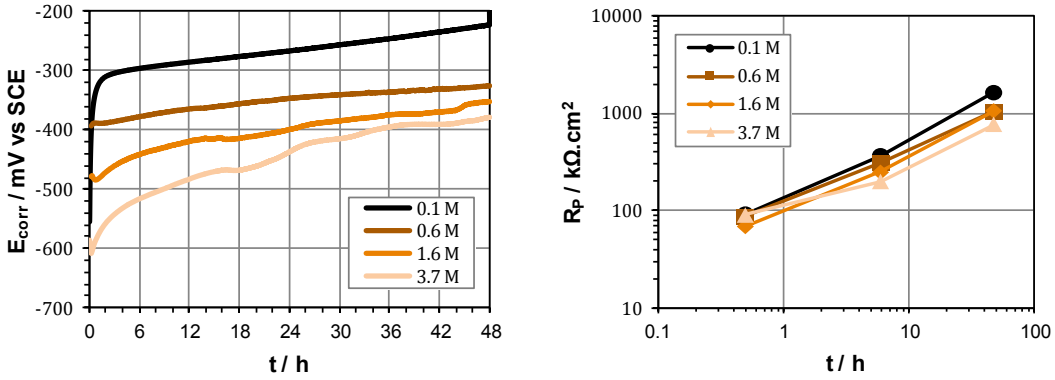

(a) **(b)**

Figure 4.2 Naturally grown passive films on LDX 2101 stainless steel after immersion in 0.1 M, 0.6 M, 1.6 M, and 3.7 M solutions for up to 2 days. (a) Corrosion potential E_{corr} and (b) polarization resistance R_P after 30 minutes, 6 hours, and 2 days for naturally grown passive films after immersion of the LDX 2101 stainless steel in the 0.1 M, 0.6 M, 1.6 M, and 3.7 M solutions (log-log plot). See Table 2.2 for the compositions of the solutions.

The protective character of the passive films was also evaluated by measuring their polarization resistances, i_{corr}, after 30 minutes, 6 hours, and 2 days immersion for the 0.1 M, 0.6 M, 1.6 M, and 3.7 M solutions. For the 0.1 M solution, the polarization resistance was 90 kΩ.cm^2 after 30 minutes, and 199 kΩ.cm^2 after 6 hours. After 2 days the value went up to 771 kΩ.cm^2. We observed similar increases for the other solutions (Figure 4.2.b).

4.2. Cyclic potentiodynamic polarization

Polarization of low-carbon steel has shown to be a powerful method useful to understand the stability of the iron oxides for the low-carbon steel Chapter 3, section 3. A similar analysis was carried for the LDX 2101 stainless steel. Starting the cyclic potentiodynamic polarization at -1300 mV versus SCE, an intense negative current was measured for the 0.1 M, 0.6 M, 1.6 M, and 3.7 M solutions (Figure 4.3).

All oxide species present on the electrodes were reduced, and a strong negative current indicated the hydrolysis of water for potentials lower than $E_0 = -244 - 59pH\ [mV\ vs\ SCE]$ (Pourbaix 1974). With increasing potential, the current density during the anodic scan first increased, and went across three oxidation peaks (labeled I,

II, and III) attributed to iron oxidation as described in Chapter 3, section 3. The steel then entered the passive state where the current density stabilized around a small value. Above 0mV vs SCE, a fourth oxidation peak occurred, which is attributed to the oxidation of chromium(III)-oxide (Cr_2O_3) into chromate ion (CrO_4^{2-}). The pH depends of the position of this peak is predicted by Nernst potential:

$$E_0\left(Cr_2O_3 \rightarrow CrO_4^{2-}\right) = 1067 - 99pH + 20\log(CrO_4^{2-})\ [mV\ vs\ SCE]$$

(Pourbaix 1974).

Finally, below +500 mV, the potential reached the potential of electrolysis of water $E_0 = 984 - 59pH\ [mV\ vs\ SCE]$ (Pourbaix 1974), and the current density rose significantly. On the cathodic scan, starting from +500 mV vs SCE, the current density was zero since the passive film formed during the anodic scan protected the steel. Then, at lower potentials, three major peaks (labeled V, VI, and VII, Figure 4.3) indicated the reduction of the oxides formed during the anodic scan. The peaks labeled from I to VII saw their positions and relative areas changing with increasing alkalinity. The peak positions decreased linearly with pH as predicted by Pourbaix (Pourbaix 1974). All peaks intensities remained comparable from one solution to another, including for the oxidation peak II, and except for the oxidation peak IV. The relative importance of the oxidation peak IV, together with the formation soluble chromium oxide CrO_4^{2-}, significantly increased with the alkalinity of the solution.

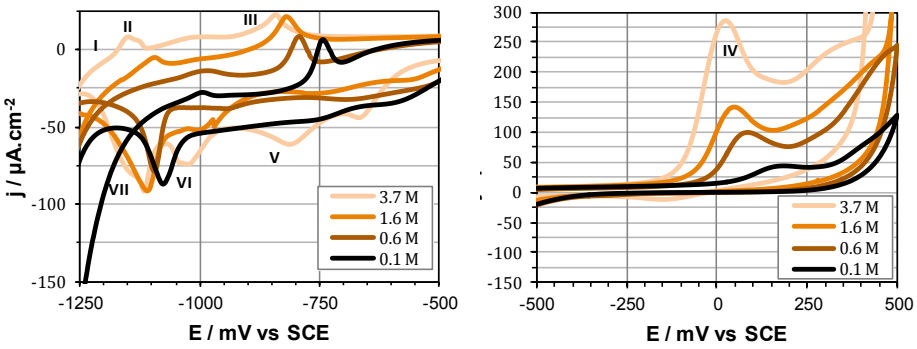

Figure 4.3 Cyclic voltammograms for LDX 2101 stainless steel at a sweep-rate of 2 mV/s when immersed in the 0.1 M, 0.6 M, 1.6 M, and 3.7 M solutions. See Table 2.2 for the compositions of the solutions. On the anodic scan, they showed four oxidation peaks - labeled I, II, III, and IV. On the cathodic scan, after a zero current density region, they showed three reduction peaks - labeled V, VI, and VII.

4.3. Depth profile of the passive film

Synchrotron-based XPS allows for non-invasive probing of the oxide film at various depths. The oxide content was measured by scanning the region from 39 eV to 64 eV, measuring the Fe3p, and Cr3p peaks (respectively at 52.9 eV, and 41.9 eV). By changing the incident photon energy from 300 eV, to 500 eV, and to 700 eV, the probing depth increased from 2 nm, to 3 nm, to 4 nm. The technique has been used to characterize the film grown in the 0.1 M and 3.7 M solutions after a 2-day immersion (Figure 4.4). To compensate the changes in photon flux, the spectra in Figures 4.4 have been normalized by the intensity of the chromium(III)-oxide peak at 44 eV.

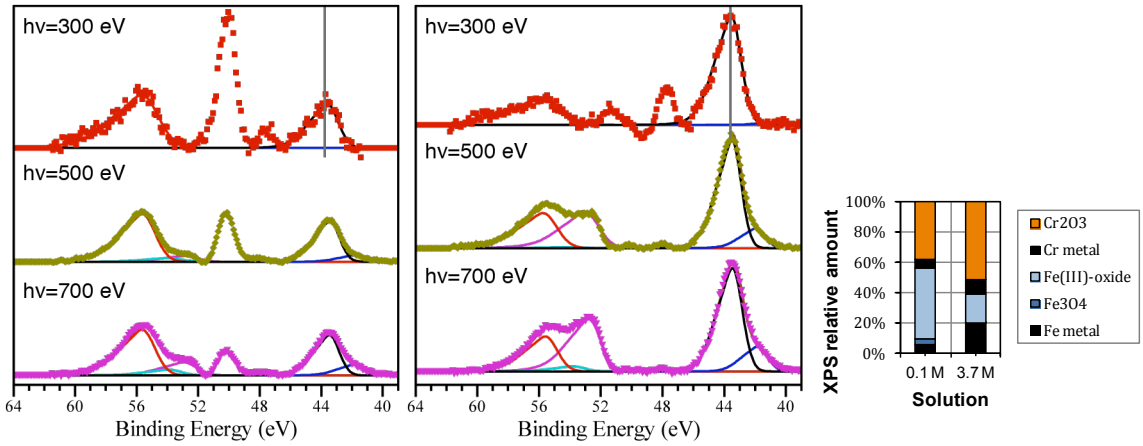

(a) 0.1 M solution after 2 days **(b)** 3.7 M solution after 2 days **(c)**

Figure 4.4 Fe3p and Cr3p XPS peaks for LDX 2101 stainless steel immersed for 2 days. (a) in the 0.1 M solution, and (b) in the 3.7 M solution. Photon energies 300 eV (red, on top), 500 eV (green, middle), and 700 eV (purple, bottom). Fe3p XPS peaks at 52.9-55.6 eV, Mn3p at 50.1 eV, and Cr3p at 41.9-43.6 eV. (c) Oxide relative amounts from XPS. Photon energy 500 eV.

For the passive film grown in the 0.1 M solution for 2 days (Figure 4.4.a), the importance of the chromium metal peak (41.9 eV), and iron metal peak (52.9 eV) was decreasing with increasing photon energy; the bare metal is laying underneath the oxide film. With photon energy 300 eV, the XPS spectrum was probing the outer-part of the passive film, and only the chromium(III)-oxide and iron(III)-oxide peaks were observed. Chromium was accounting for 48% of the alloy interface, and chromium oxide for 42% of the total oxide film.

Similarly, for the film grown after immersion for 2 days in the 3.7 M solution (Figure 4.4.b), the importance of the chromium metal peak (41.9 eV), and iron metal peak (52.9 eV) was decreasing with increasing photon energy. Chromium was accounting for 33% of the alloy interface, and chromium oxide for 73% of the total oxide film.

In the 3.7 M solution, the iron metal peak was stronger relative to the oxides compared to the film grown in the 0.1 M solution. This indicated a thinner iron oxide film

in the 3.7 M solution than in the 0.1 M solution. In both solutions the alloy interface was enriched in chromium: 21% of the alloy is made of chromium (Table 2.1), but at the alloy interface there is 48% of chromium (0.1 M solution) and 33% for the 3.7 M solution. The enrichment in chromium oxide in the oxide film was significantly more important in the 3.7 M solution (73%) than in the 0.1 M solution (42%).

4.4. Discussion

With time, the open circuit potential of the LDX 2101 duplex stainless steel grew to more positive values (Figure 4.2.). After 2 days, the chromium oxide content in the passive film increased, and the iron(III)-oxide content decreased (Figure 4.1.a, and 4.4.c). Addari *et al.* observed a similar evolution of the potential and comparable trends for the oxide content when they immersed stainless steel in 0.1 M NaOH for 1 day (Addari, Elsener, and Rossi 2008). Schmutz *et al.* suggested that the chromium oxide was present in the inner-part of the film formed on the Fe-25Cr alloy (Schmutz and Landolt 1999). However, at 300 eV, chromium(III)-oxide and iron(III)-oxide were detected, but not chromium, iron, or iron(II)-oxide. At 300 eV, the probing depth of XPS is smaller than at 500 and 700 eV, therefore it indicated that chromium(III)-oxide was present in the outermost part of the film (Figure 4.4.a).

After 30 minutes of immersion, the polarization resistance of the passive film formed in the 0.1 M, 0.6 M, 1.6 M, and 3.7 M solutions remained constant with increasing alkalinity of the solution (Figure 4.1.a.). This indicated that the LDX 2101 stainless steel passive film stayed as protective at higher alkalinities. XPS analysis of the Fe 3p peak and the Cr 3p peaks showed that the film formed after 30 minutes contained less iron oxides and a constant amount of chromium oxide with increasing alkalinity of the solution (Figure 4.1.a.). This indicated that, even if the film was depleted in iron oxides at higher alkalinities, it remained protective thanks to the chromium oxides. No significant differences in corrosion performance were observed during the 2 days of immersion in the 0.1 M, 0.6 M, 1.6 M, and 3.7 M solutions, whereas for the low-carbon steel, films formed at higher alkalinities became noticeably less protective (Chapter 3).

Differences in corrosion behavior for the low-carbon steel have been arising from the solubility of the iron(II)-oxides into $HFeO_2^-$ at high alkalinity. On the cyclic votammograms (Figure 3.4), differences were seen in the increasing importance of the oxidation peak II relative to the others. For the LDX 2101 stainless steel, we did not observed any increase of the peak II intensity with increasing alkalinity of the solution (Figure 4.3). It implies that no significant amount of soluble iron oxide went into solution while crossing peak II. Chromium(III)-oxide (Cr_2O_3) is produced at low potentials (Pourbaix 1974), and it was very likely to have formed before the potential came across the potential for soluble iron(II)-oxide to form. The chromium oxide layer that formed on the steel rebar prevented the iron from oxidizing in large quantities, and most particularly hindered the formation of the soluble dihypoferrite ions $HFeO_2^-$. This was confirmed by a much higher chromium oxide content in the 3.7 M solution than in the 0.1 M solution after 2 days (Figure 4.4.c). Chromium oxide is balancing out for the dissolved iron oxide that went into solution, and it resulted in a stabilized corrosion performance.

4.4.1. Different layering models

The XPS analysis has identified five different species in the passive film forming on LDX 2101 stainless steel: two iron oxides (Fe_3O_4 and iron(III)-oxides), one chromium oxide (Cr_2O_3), and two metals (Fe^0 and Cr^0). Their layering order remained unknown and two hypotheses were investigated: (I) chromium oxide formed underneath the other oxides and (II) chromium oxide formed next to the other oxides.

Hypothesis I: chromium oxide formed underneath the other oxides

The Pourbaix diagram suggests that, starting from a low potential, Cr_2O_3 is most likely to form first, followed by Fe_3O_4, and finally iron(III)-oxides, forming successive layers of Cr_2O_3, Fe_3O_4 and iron(III)-oxide on top of iron and chromium metals (Figure 4.5). The computed intensities are as follows:

$$\begin{cases} I'_{Fe(III)} = I_0\left(1 - exp\left(-d_3 \middle/ \lambda_{Fe(III)}\right)\right) \\ I'_{Fe_3O_4} = I_0 exp\left(-d_3 \middle/ \lambda_{Fe(III)}\right)\left(1 - exp\left(-d_2 \middle/ \lambda_{Fe_3O_4}\right)\right) \\ I'_{Cr_2O_3} = I_0 exp\left(-d_3 \middle/ \lambda_{Fe(III)}\right) exp\left(-d_2 \middle/ \lambda_{Fe_3O_4}\right)\left(1 - exp\left(-d_1 \middle/ \lambda_{Cr_2O_3}\right)\right) \\ I'_{Fe} = (1-\alpha) I_0 exp\left(-d_3 \middle/ \lambda_{Fe(III)}\right) exp\left(-d_2 \middle/ \lambda_{Fe_3O_4}\right) exp\left(-d_1 \middle/ \lambda_{Cr_2O_3}\right) \\ I'_{Cr} = \alpha I_0 exp\left(-d_3 \middle/ \lambda_{Fe(III)}\right) exp\left(-d_2 \middle/ \lambda_{Fe_3O_4}\right) exp\left(-d_1 \middle/ \lambda_{Cr_2O_3}\right) \end{cases}$$

where $I' = I / \sigma N \lambda$ is the reduced peak intensity, with I the peak area, σ the photoionization cross-section, N the volume density, and λ the IMFP. It is then possible to solve the system into:

$$\begin{cases} \alpha = I'_{Cr} \Big/ I'_{Fe} + I'_{Cr} \\ d_1 = \lambda_{Cr_2O_3} ln\left[\alpha \, I'_{Cr_2O_3} \Big/ I'_{Cr} + 1\right] \\ d_2 = \lambda_{Fe_3O_4} ln\left[\left(1 - exp\left(-d_1 \middle/ \lambda_{Cr_2O_3}\right)\right) I'_{Fe_3O_4} \Big/ I'_{Cr_2O_3} + 1\right] \\ d_3 = \lambda_{Fe(III)} ln\left[\left(1 - exp\left(-d_2 \middle/ \lambda_{Fe_3O_4}\right)\right) I'_{Fe(III)} \Big/ I'_{Fe_3O_4} + 1\right] \end{cases}$$

The values of α, d_1, d_2, and d_3 were computed with tabulated values from Table A.2 and the XPS peak areas (Figure 4.5).

The total thickness of the film decreased with increasing alkalinity: from 22 Å in the 0.1 M solution, it dropped to 15 Å in the 3.7 M solution. Most of the film is constituted of chromium oxide, and the thickness of its layer remained at 14 Å for the 0.1 M, 0.6 M, and 1.6 M solutions, with a drop to 10 Å for the 3.7 M solution. Conversely, the thickness of the iron oxide layer constantly decreased with alkalinity. From 8 Å in the

0.1 M solution, it dropped to 5 Å in the 3.7 M solution. A similar behavior had been observed for the passive film formed on low-carbon steel (Chapter 3).

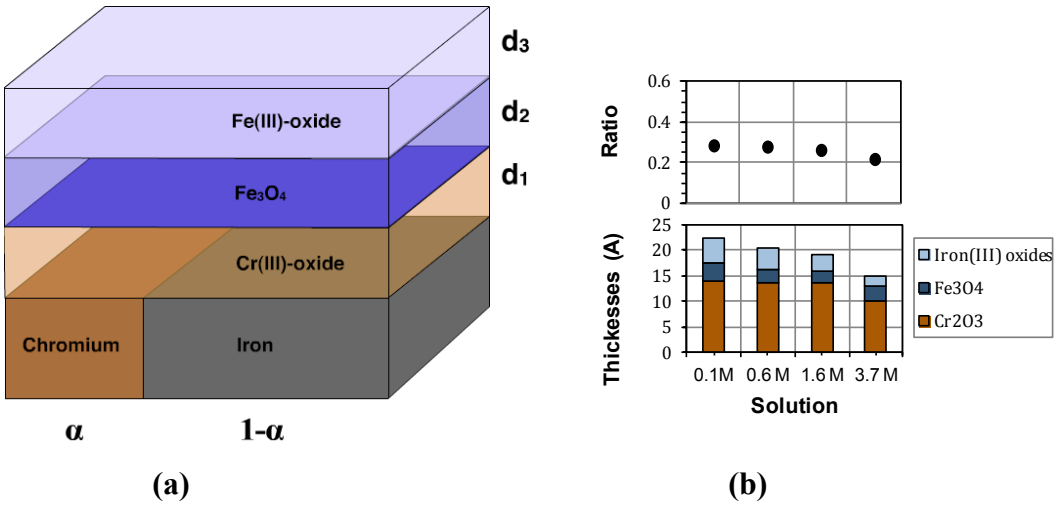

Figure 4.5 Passive film formed on LDX 2101 stainless steel after immersion in 0.1 M, 0.6 M, 1.6 M, and 3.7 M solutions for 30 min. Hypothesis in which the chromium oxide layer formed underneath the iron oxides layers. (a) Diagram, and (b) results. The thicknesses were noted d_1, d_2, d_3, and the chromium metal content ratio α.

Hypothesis II: chromium oxide formed next to the other oxides

About a fifth of the LDX 2101 stainless steel surface is composed of chromium (Table 2.2). While immersed in the alkaline solutions, chromium and iron oxidize and participate in the formation of the passive film. Chromium oxide was detected in the outer-part of the film (Figure 4.4). In this hypothesis, the two oxide layers are growing next to each other (diagram in Figure 4.6). The computed intensities are as follows:

$$\begin{cases} I'_{Fe(III)} = (1-\beta)I_0\left(1-exp\left(-d_3/\lambda_{Fe(III)}\right)\right) \\ I'_{Fe_3O_4} = (1-\beta)I_0 exp\left(-d_3/\lambda_{Fe(III)}\right)\left(1-exp\left(-d_2/\lambda_{Fe_3O_4}\right)\right) \\ I'_{Cr_2O_3} = \beta I_0\left(1-exp\left(-(d_2+d_3)/\lambda_{Cr_2O_3}\right)\right) \\ I'_{Fe} = (1-\alpha)I_0 exp\left(-d_3/\lambda_{Fe(III)}\right) exp\left(-d_2/\lambda_{Fe_3O_4}\right) \\ I'_{Cr} = \alpha I_0 exp\left(-d_3/\lambda_{Fe(III)}\right) exp\left(-d_2/\lambda_{Fe_3O_4}\right) \end{cases}$$

where $I' = {}^{I}/_{\sigma N \lambda}$ is the reduced peak area, with I is the peak area, N the photoionization cross-section, N the volume density, and λ the IMFP. α is the chromium content in the metal, and β the chromium content in the oxide film. It is finally solved into:

$$\begin{cases} \alpha = {}^{I'_{Cr}}/_{I'_{Fe} + I'_{Cr}} \\ \beta = {}^{I'_{Cr_2O_3}}/_{I'_{Fe_3O_4} + I'_{Fe(III)} + I'_{Cr_2O_3}} \\ d_2 = \lambda_{Fe_3O_4} ln\left[1 - {}^{\alpha}/_{1-\beta} \, {}^{I'_{Fe_3O_4}}/_{I'_{Fe}} + 1\right] \\ d_3 = \lambda_{Fe(III)} ln\left[\left(1 - exp\left({}^{-d_2}/_{\lambda_{Fe_3O_4}}\right)\right) {}^{I'_{Fe(III)}}/_{I'_{Fe_3O_4}} + 1\right] \end{cases}$$

The value of α, β, d_2, and d_3 were computed with tabulated values from Table A.2 and the XPS peak areas (Figure 4.6).

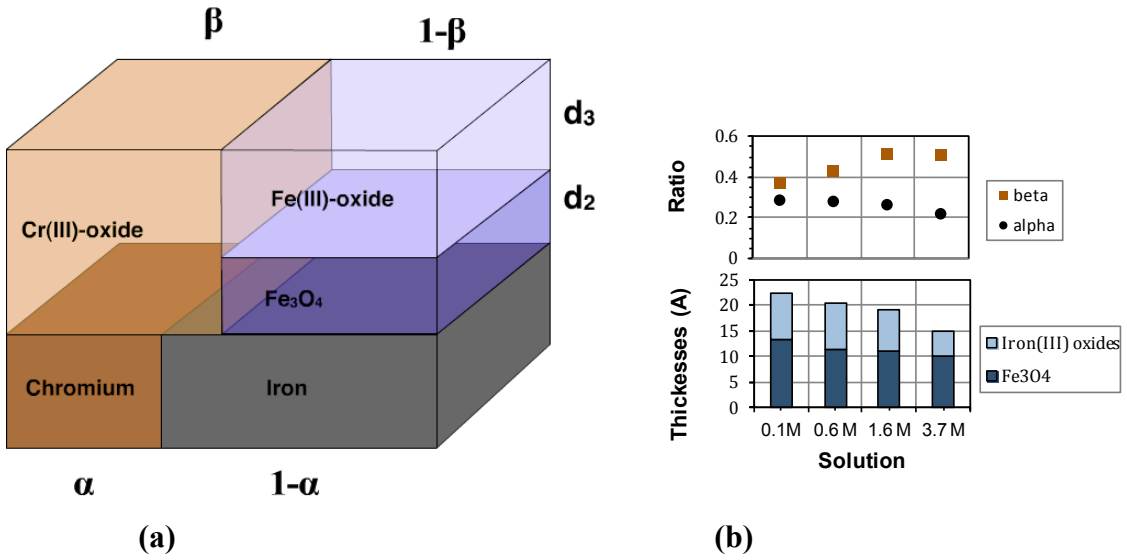

Figure 4.6 Passive film formed on LDX 2101 stainless steel after immersion in 0.1 M, 0.6 M, 1.6 M, and 3.7 M solutions for 30 min. Hypothesis in which the chromium oxide layer formed next to the iron oxide layers. (a) Diagram, and (b) results. The thicknesses were noted d_2, d_3, and the metal content ratio α, and the oxide content ratio β.

In the hypothesis the iron and chromium oxides are growing side by side (Figure 4.6), the results for the chromium content in the steel and the thickness of the film were very similar with the results from the hypothesis I where the chromium oxide layer is growing underneath the iron oxides (Figure 4.5). The chromium oxide content in the film increased with increasing alkalinity: from 37% in the 0.1 M solution to 51% in the 1.6 M and 3.7 M solutions.

4.5. Summary

The corrosion resistance of the LDX 2101 duplex stainless steel increases with time, and stabilizes after an immersion of about 2 days. The passive film becomes thicker with time, and gets enriched in iron(III)-oxide and chromium(III)-oxide. For solutions with higher alkalinities, spanning from 0.1 mol/L to 3.7 mol/L hydroxide, the enrichment in chromium(III)-oxide becomes more important, and no significant amount of iron(II)-oxide is dissolved in solution. It results in improved corrosion performances, with comparable resistances even at higher alkalinities.

X-ray photoelectron non-invasive depth profiling allows the validation of layering hypotheses for the passive film forming on LDX 2101 duplex stainless steel. Chromium(III)-oxide is detected in the outer-part of the passive film, in similar amounts as in deeper parts of the film. Therefore chromium oxide and iron oxide layers are most likely to grow side by side. This hypothesis allows quantifying the thicknesses and relative amounts in the film. From 30 minutes to 2 days, the film grows with about 40% of chromium(III)-oxide when immersed in the 0.1 mol/L hydroxide solution. Conversely, in the 3.7 mol/L hydroxide solution, the film gets enriched from 51% of chromium(III)-oxide after 30 minutes to 72% after 2 days. Furthermore, after 2 days, the film is 2.8-nm thick in the 0.1 mol/L hydroxide solution, and 1.8-nm thick in the 3.7 mol/L solution.

These results are in strong contrast with the results found for the low-carbon steel. Chromium(III)-oxide seems to lessen the solubility of iron(II)-oxides at high alkalinities, and therefore the passive films forming on LDX 2101 duplex stainless steel are stronger and more suited for reinforced inorganic polymer concrete structures. Whether the high-chromium content of LDX 2101 duplex stainless steel (21%) is necessary, still needs to be investigated, and cheaper alternatives, like ferritic stainless steels, should be considered. The lower chromium content of ferritic stainless steels, upon enrichment of the passive layer in chromium(III)-oxide, may form passive films that are strong enough to sustain highly alkaline environments.

Chapter 5: *In-situ* three-dimensional monitoring of steel corrosion in cement paste

Stainless steels have shown to perform better than low-carbon steel in environments with higher alkalinities (Chapter 3 and 4). They formed stronger passive films, and they are expected to have a longer corrosion initiation period. However, in salt contaminated environments for example, corrosion pits are likely to form, and active corrosion eventually takes place (Bertolini et al. 1996). Each steels present different corrosion mechanisms, and their corrosion can harm the structure in different ways. The active corrosion behavior of three different types of steel was studied: low-carbon steel (ASTM A36), Top12 ferritic stainless steel (UNS S41000), and LDX 2101 duplex stainless steel (UNS S32101).

The accumulation of corrosion products at the steel/concrete interface and the mechanism of corrosion-induced crack formation are of major interest. However the only available results were obtained by either causing damage to the samples (Zhao et al. 2012) or making external observations (Andrade, Alonso, and Molina 1993). Micro-computed tomography (μCT) offers a non-destructive tool to monitor the evolution of corrosion inside concrete. Reinforcing bars were first thinned down to 0.5 mm-diameter cylinders, and then they were embedded at the center of 5 mm-diameter cement paste cylinders. An external current was applied to the steel reinforcing bar in order accelerate corrosion and obtain comparable amounts of corrosion for all steels.

5.1. Galvanostatic corrosion

Galvanostatic corrosion of the steel reinforcement was performed by imposing a constant current density, i_G, of 5 mA/cm^2 during comparable amounts of time and measuring the potential of the steel, E_G, with respect to the reference. This current density is significantly higher than would naturally occur (Andrade and González 1978). However, since the aim of the research is to compare the propagation phase of three types of steel in cement paste (carbon and stainless steel) the applied current density is considered to be adequate for the purpose. Additionally, since the chosen steels and cement pastes were of good quality, using higher current density instead of compromising the quality of cement paste, forcing its resistance to be unrealistically weak, was considered to be a better choice to obtain results in a reasonable time frame. The potential of the steels, E_G, was measured to evaluate its corrosion stage (Figure 5.1). At times t_0, t_1, t_2, and t_3, the samples were taken out of solution and imaged by μCT.

For the 3 hours of the galvanostatic corrosion, the three steels showed different behaviors. For the low-carbon steel sample, the potential was steady at +1V vs SCE for the first 45min after which it suddenly dropped. It then remained constant at +0.2V vs SCE before dropping once again after 1 hour and 20 minutes. At the end, it stabilized at -0.2V vs SCE. Then, for the Top12 steel sample, the potential stayed at +1.6V vs SCE up for 1 hour. After that it slowly decreased and reached its low value at +0.25V vs SCE after 2 hours. Finally, for the LDX 2101 steel sample, the potential started at a high voltage of about +14 V vs SCE. As to not damage the galvanostat, the current density

was reduced to 0.5 mA/cm^2 after the first 30 min; the potential decreased to about +1.5 V vs SCE for the remainder of the experiment.

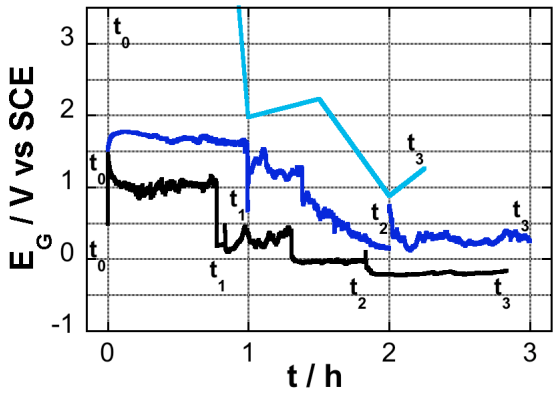

Figure 5.1 Potential of the steel during galvanostatic corrosion at an anodic current density of 5 mA/cm2. Low-carbon steel (black), Top12 steel (dark blue), and LDX 2101 stainless steel (lighter shade of blue).

5.1.1. Corrosion products and crack patterns in the matrix

At the specified times t_0, t_1, t_2, and t_3 indicated in Figure 5.1, the samples were taken out of the electrochemical cell to be imaged in the µCT instrument. Once reconstructed, data were visualized through reconstructed tomograms (Figure 5.2). At a given height, z_0, the value of the linear attenuation field, $\mu(x, y, z_0)$, is displayed as a grayscale value in a (x, y)-image. In general for x-rays, the higher the density, the higher is the linear attenuation coefficient. In Figure 5.2, steel was the denser phase and showed in white circular areas, at the center of the sample. The cement paste is less dense and showed in grey, all around the reinforcing bar. Within the cement paste, the unhydrated cement particles are denser than the hydration products, which showed in lighter shade of grey. Air has zero density and showed in black areas, all around the circular sample, but also in the air voids inside the cement paste. Finally, when active corrosion started, the corrosion products are denser than the cement paste but less dense than steel, so the corrosion products showed in light grey similar to the unhydrated cement particles. The former were however distinguished from the latter by comparing the images before and after corrosion occurred.

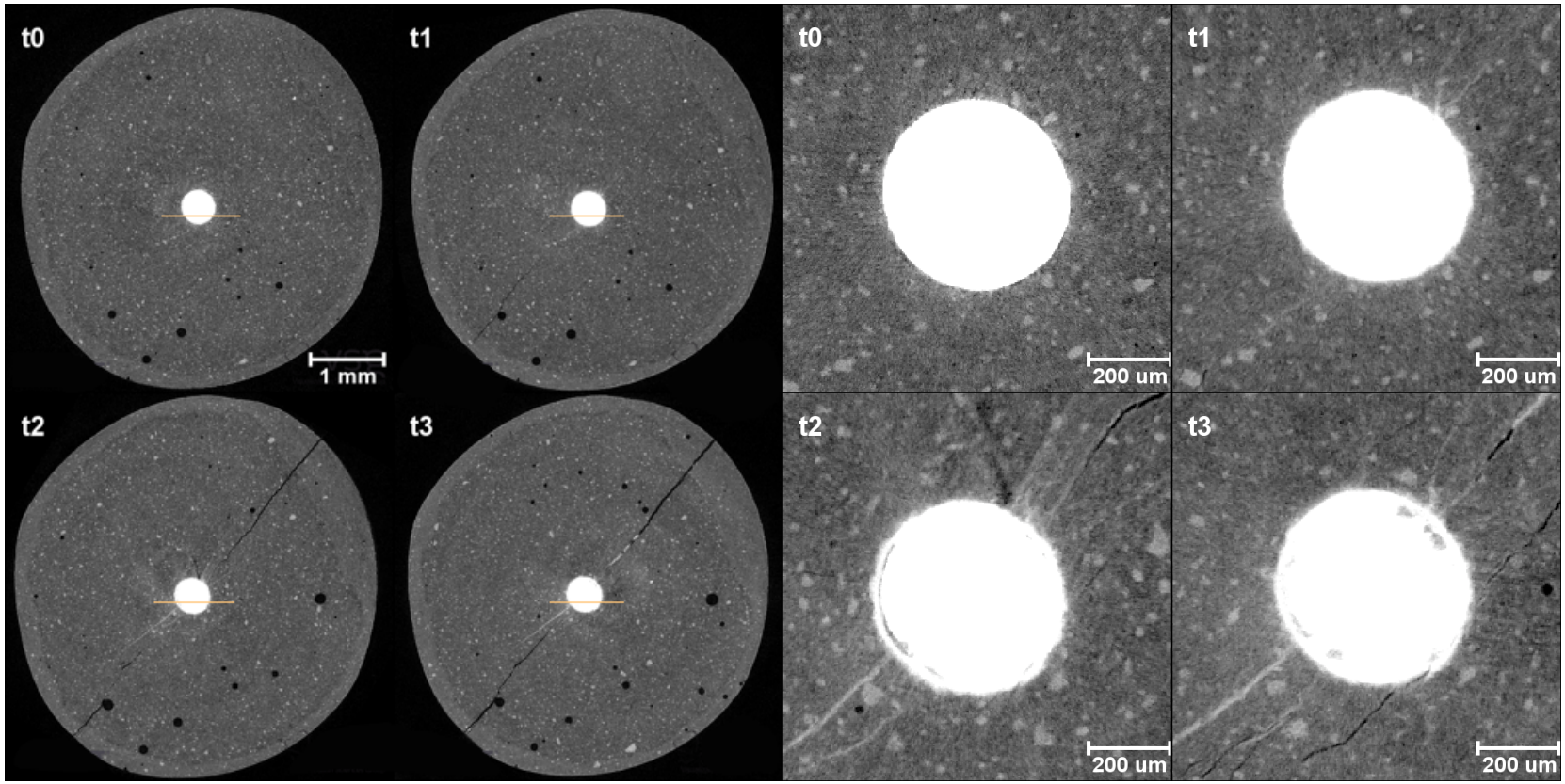

Figure 5.2 Reconstructed tomograms of the low-carbon steel sample at times t_0, t_1, t_2, and t_3. See Figure 5.1 for the definition of the times. Horizontal lines across the reinforcement indicate the location of the attenuation profiles (Figure 5.11). Images with higher magnification are shown on the right.

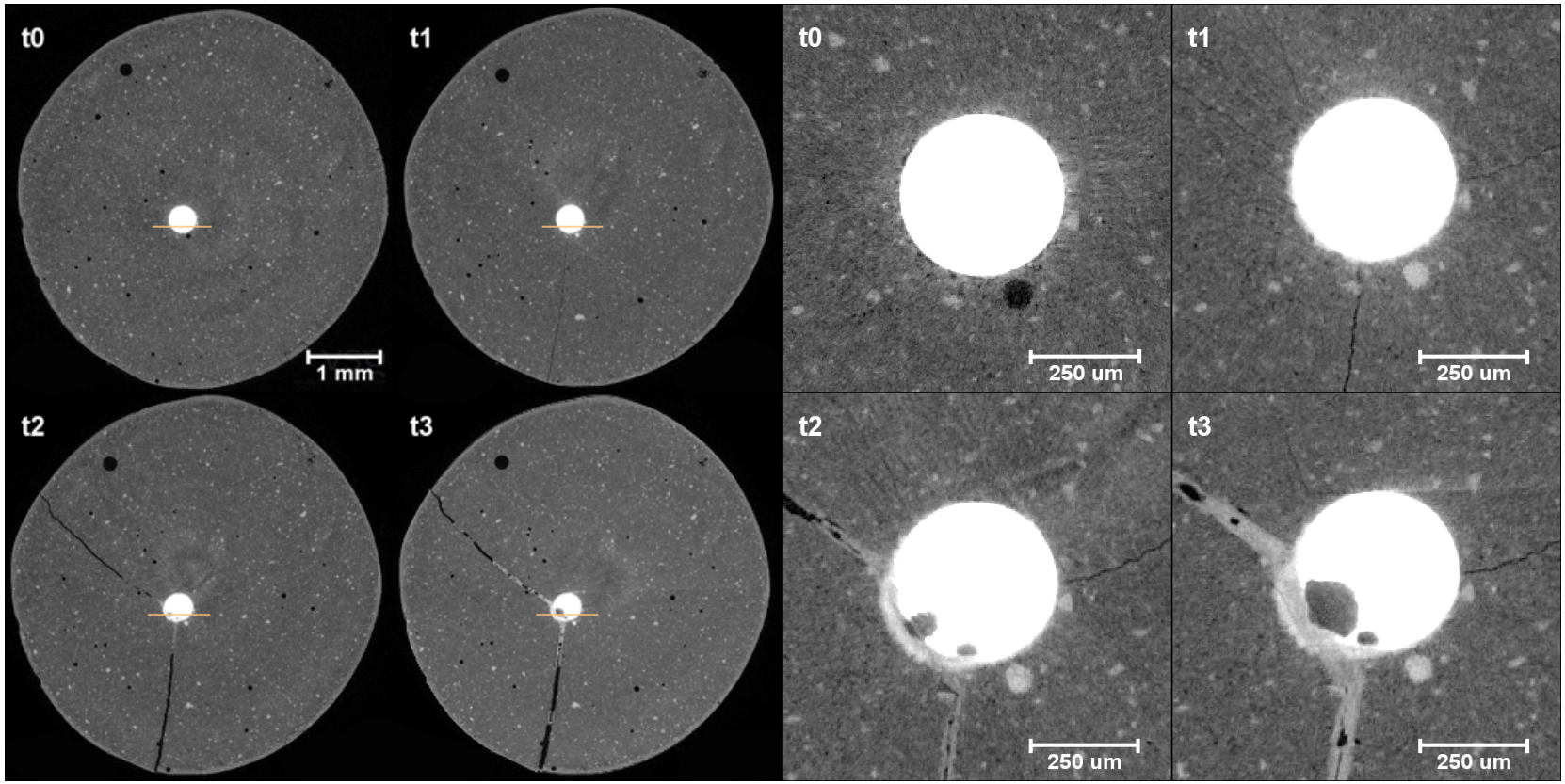

Figure 5.3 Reconstructed tomograms of the Top12 steel sample at times t_0, t_1, t_2, and t_3. See Figure 5.1 for the definition of the times. Horizontal lines across the reinforcement indicate the location of the attenuation profiles (Figure 5.11). Images with higher magnification are shown on the right.

The same location in the samples was scanned at different times. This was made possible thanks to μCT, since the sample did not have to be cut open in order to observe the corrosion products. At t_0 the reconstructed tomogram of low-carbon steel sample showed the round disk of the steel reinforcing bar, very close to the center of the cement paste disk (Figure 5.2). Small air voids were present in the cement paste, and few bigger air voids at the bottom left part of the cement paste. Between t_0 and t_1, a radial crack formed in the cement paste. It then grew larger at times t_2 and t_3, and another radial crack formed on the opposite side between t_1 and t_2. At the end of the experiment (time t_3), cracks were 23- and 27 μm wide at the outer-surface of the cement paste. While the steel reinforcing bar in the center lost some of its cross-sectional area, corrosion products accumulated at the steel/cement paste interface, on the faces of the cracks, and on the wall of the air voids surrounding the steel reinforcing bar. In the bottom left quarter, corrosion products propagating from the steel surface could be observed at times t_2 and t_3, without any visible crack reaching out the surface. The corrosion products accumulated at the surface of the steel in a homogeneously distributed layer. At the end of the experiment (time t_3), the corrosion layer was 40-μm thick.

At t_0, the reconstructed tomograms for the Top12 steel sample showed the steel reinforcing bar position was slightly shifted from the center toward the lower left of the cement paste matrix (Figure 5.3). Many air voids smaller than 100 μm were homogeneously distributed in the cement paste. Between t_0 and t_1, a radial crack formed in bottom part of the cement paste. It then grew larger at times t_2 and t_3, and another radial crack formed between t_1 and t_2 at a +120° angle (clockwise) from the first one. At the end of experiment (time t_3), cracks were 27- and 74 μm wide on the outer-surface of the cement paste. The corrosion products formed only on one side of the steel reinforcing bar, in a region delimitated by two of the radial cracks. They accumulated to a 73-μm-thick layer. In comparison with the low-carbon steel, the Top12 steel formed a thicker corrosion product layer and cracks opened wider on the outer-surface of the cement paste.

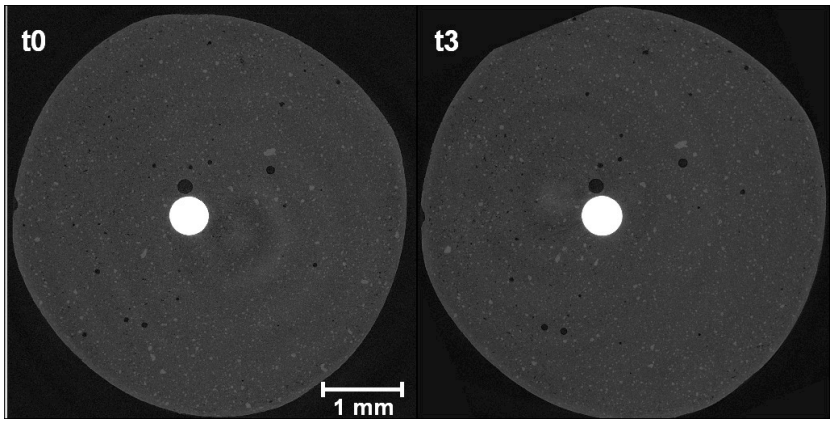

Figure 5.4 Reconstructed tomograms of the LDX 2101 stainless steel sample at times t_0, and t_3. See Figure 5.1 for the definition of the times.

The LDX 2101 stainless steel reinforcing bar was placed in an slightly eccentric position with respect to the cement paste (Figure 5.4). From t_0 to t_3, no noticeable changes appeared in the reconstructed tomograms.

The widths of the cracks developing on low-carbon steel and Top12 steel were measured at time t_3 (Figure 5.5). The measurement was conducted on a plane orthogonal of the steel rebar, using the reconstructed tomograms from Figure 5.2 and 5.3.

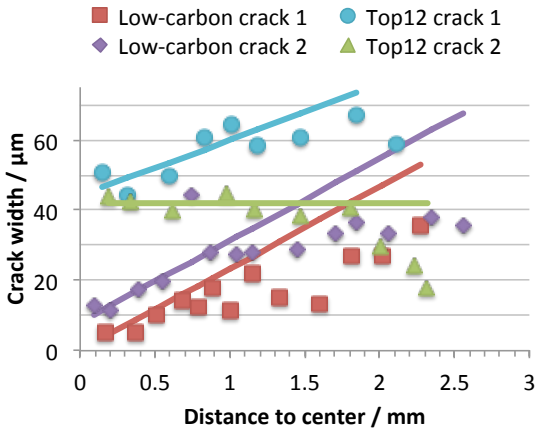

Figure 5.5 Crack width as a function of the distance to the steel/cement paste interface. Measurement for the two major cracks in the low-carbon steel and the Top12 steel samples at time t_3. Linear approximations are plotted for the region next to the steel interface.

Next to the steel interface, the crack widened linearly with the distance to center. The second crack in the Top12 steel sample is an exception; its width remained constant. The widening rates for the two cracks in the low-carbon steel sample are comparable, while for the Top12 steel sample it was lower. For distances greater then 1 mm, the cracks' widening was less important, and it became almost constant.

5.1.2. Morphology of the corroded steel reinforcing bar

In this experiment, steel was the material with the greatest linear attenuation coefficient (around 20 cm^{-1} at 45 keV). A binary representation of the steel reinforcing bar was obtained by segmenting out the parts with the highest greyscale values, i.e., keeping all voxels (x, y, z) for which the linear attenuation coefficient $\mu(x, y, z)$ is greater than 15 cm^{-1}. Segmented images of the low-carbon steel reinforcing bars at times t_0, t_1, t_2 and t_3 are shown on Figure 5.6, Top12 steel in Figure 5.7, and LDX 2101 steel in Figure 5.8.

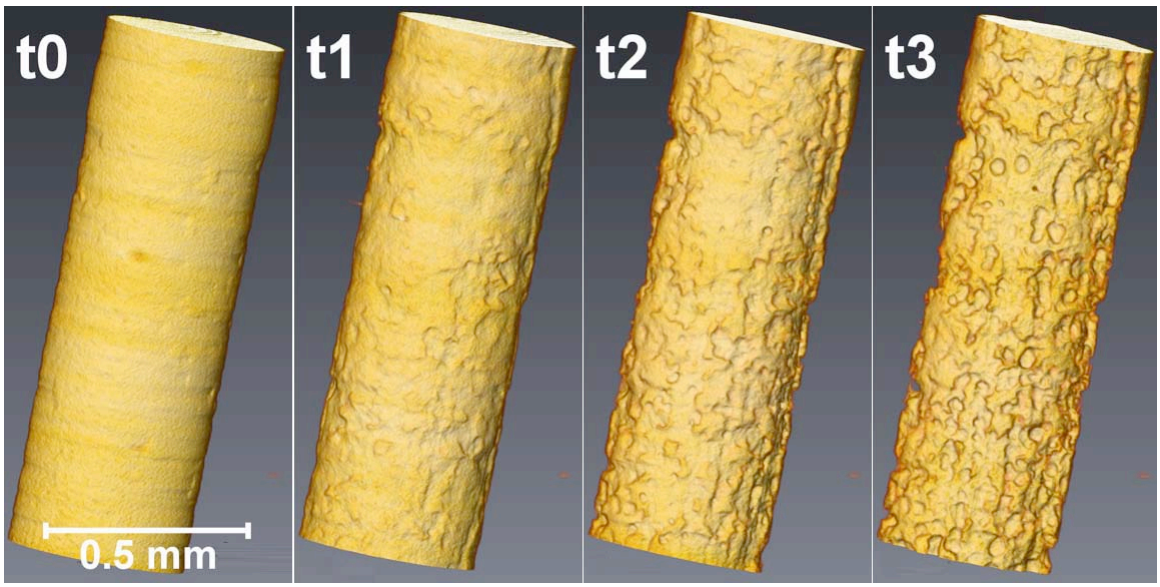

Figure 5.6 Segmented surface of the low-carbon steel sample from t_0 to t_3.

From an overall smooth surface at t_0, the low-carbon steel sample showed some homogeneously distributed small pits (Figure 5.6) with sizes at the limit of the resolution of the instrument (pixel size is 3.3µm). Then, after impressing an anodic current, between t_0 and t_1, large areas started to corrode away from the surface of the steel. Corrosion grew gradually bigger at times t_2 and t_3. Pits were hollow and connected in groups, causing general corrosion of the steel.

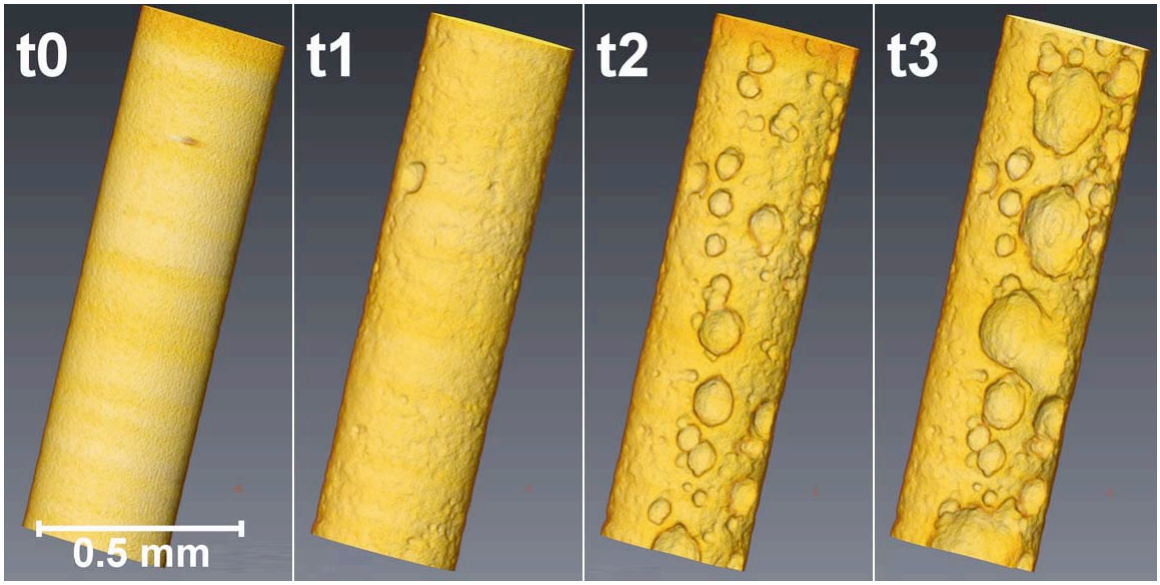

Figure 5.7 Segmented surface of the Top12 steel sample at times from t_0 to t_3.

Before galvanostatic corrosion started, the surface of the Top12 steel presented a round and smooth surface (Figure 5.7). Between t_0 and t_1, only one pit initiated in the upper part of the sample, while the rest of the surface became slightly rougher. Between t_1 and t_2, the first pit did not grow bigger, and many more pits nucleated and grew. Finally, between t_2 and t_3, few pits grew much larger. At t_3, only a quarter of the surface of the reinforcing bar showed signs of corrosion, causing localized loss of steel. In comparison to low-carbon steel, pits that formed on the Top12 steel were deeper and mostly disconnected. Some pits were metastable, and once formed they stopped propagating, while other pits interconnected and propagated deeper.

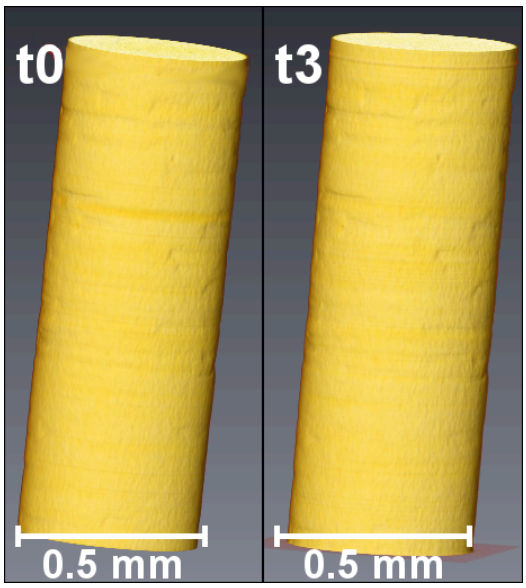

Figure 5.8 Segmented surface of the LDX 2101 steel sample at times t_0, and t_3.

The surface of the LDX 2101 steel sample was not perfectly smooth at t_0 (Figure 5.8). The flaws were most probably generated through machining. From t_0 to t_3, galvanostatic corrosion of the steel embedded in the cement paste caused no alteration of the surface.

The amount of corroded steel was measured from the segmented images of the three steels. The volume was measured using the quantification tools in the software Avizo. It was then divided by the sample length (1.3 mm), to give its average cross-sectional area, A. The measured average penetration depth, δ_m, was computed by dividing the area by the perimeter of the initial cross-section with radius, r_0. It reads:

$$\delta_m = (A_0 - A)/2\pi r_0$$

The depth of the deepest pit was also measured on the reconstructed tomograms (Table 5.1).

Table 5.1 Average penetration depth (in µm) and depth of deepest pit (in µm) during galvanostatic corrosion at an anodic current of 5 mA/cm^2

	Depth (µm)	t_0	t_1	t_2	t_3
Low-carbon	**Average penetration depth, calculated from µCT**	0	3.5	8.0	13.9
	Deepest pit, measured from µCT	8	18	46	83
Top12	**Average penetration depth, calculated from µCT**	0	1.8	5.7	10.9
	Deepest pit, measured from µCT	0	41	85	124

For the low-carbon steel sample, the deepest pit grew from 8 µm at t_0 to 83 µm at t_3. The pit at t_0 is most likely not a corrosion pit, but a machining flaw. After t_0, the deepest pit increased from 3.3 times to 4.7 times greater than the average general penetration. For the Top12 steel, the deepest pit grew from 41 µm at t_1 to 124 µm at t_3. No machining flaw was observed at t_0. It was for all cases about 6.2 times greater than the average general penetration. These two values are in the range of values from the work by Gonzalez *et al.*, where they measured the maximum penetration to be four to eight times the average general penetration (González et al. 1995).

5.1.3. Migration of the corrosion products

The Top12 sample at time t_3 was segmented in three phases: the corroded steel reinforcement, the corrosion products surrounding the reinforcing bar and migrating away along the crack, and the cracked cement paste matrix. The segmentation is shown through the hybrid image of Figure 5.9.

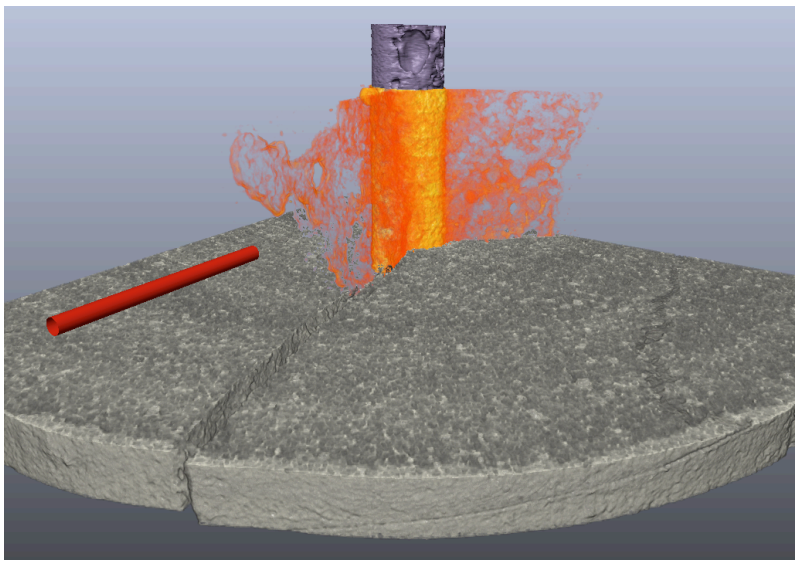

Figure 5.9 Hybrid 3D image of the Top12 steel sample at time t_3. With the hardened cement paste (grey), the corrosion products (orange and yellow), and the steel reinforcing bar (purple). The red rod on the left has been added and measures 1mm in length.

Two major cracks formed radially in the cement paste matrix, starting from the reinforcing bar and ending at the cement paste surface. The migration of the soluble corrosion product followed the crack path. The migration front was not uniform, with some parts migrating further than others. When the crack was not completely filled with corrosion products, the latter deposited on the walls of the crack. Attenuation length profiles across the cracks were obtained in order to identify the type of corrosion products (Figure 5.10).

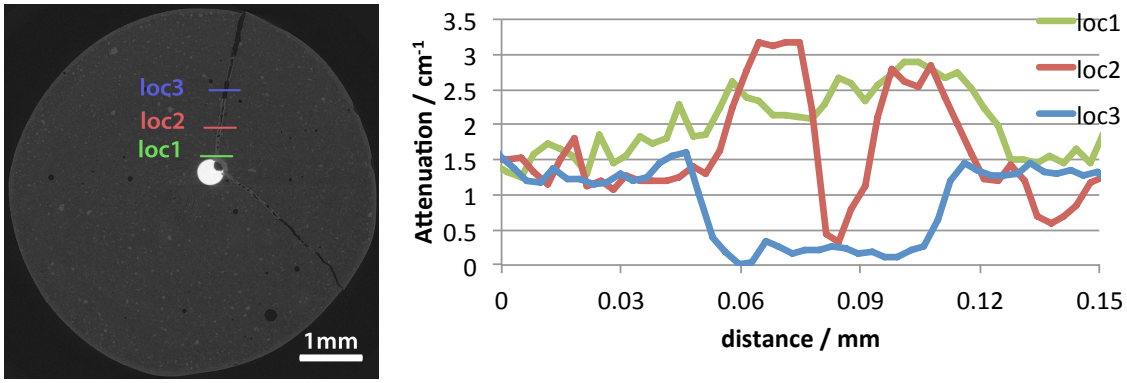

Figure 5.10 Linear attenuation profiles along a major crack on the Top12 steel at time t_3. Across the crack full of corrosion products (loc1), across the crack with corrosion products deposited (loc2), and across the empty crack (loc3).

For steel, the measured linear attenuation coefficient was 18.4 cm^{-1}, for cement paste 1.5 cm^{-1}, and for air it was 0. Next to the reinforcing bar, the cracks were filled with corrosion products (Figure 5.10 loc1). Further out, less corrosion products migrated, and corrosion products were only seen on the walls of the crack (Figure 5.10 loc2). Finally after the corrosion front, the cracks were empty of corrosion products (Figure 5.10 loc3). For the corrosion products, the linear attenuation coefficients ranged from 2 to 3.2 cm^{-1} next to the reinforcing bar, and from 2.5 to 3.3 cm^{-1} on the walls of the crack. The variations in linear attenuation coefficient from one location to another could indicate that the corrosion products might have different compositions. However the magnitude of the differences were too close to the magnitude of the noise, preventing any conclusion on that respect.

A similar procedure was applied to evaluate the dynamic of the formation of corrosion products at the interface between steel and cement paste. For the low-carbon steel at time t_0, the steel portion in the middle had a high linear attenuation coefficient of 18.4 cm^{-1}, and it sharply dropped to 1.5 cm^{-1} at the interface with the cement paste (Figure 5.11). At later times, steel was consumed and the width the of the steel portion was shortening, while corrosion products were accumulating at the interface with linear attenuation coefficients from 5 to 10 cm^{-1}.

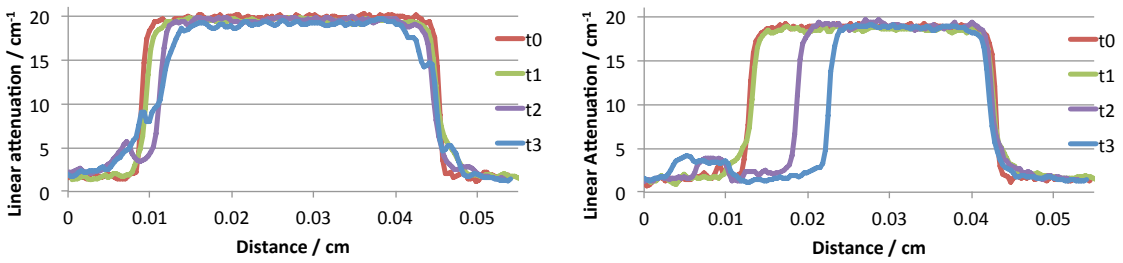

(a) **(b)**

Figure 5.11 Linear attenuation profiles across the interfaces steel/cement paste at times t_0, t_1, t_2, and t_3. (a) low-carbon steel sample, and (b) Top12 stainless steel sample. See figure 5.2 to locate the profiles on the sample.

The attenuation profile at time t_0 for the Top12 steel was similar to the low-carbon steel (Figure 5.11). At time t_1, some corrosion products formed at the interface, increasing its linear attenuation coefficient. At later times (t_2 and t_3), a corrosion pit formed and a larger portion of the steel was etched away, while corrosion products were accumulating on the outside of the cavity left by the steel.

5.1.4. Corrosion products and crack propagation

Knowing the linear attenuation coefficient of the phases present in the samples, the data was segmented into a 3D-image of the system corrosion products/crack. The voxels with linear attenuation coefficients from 0 to 1 cm^{-1} were assigned to the cracks, from 2.2 to 9 cm^{-1} to corrosion products, and above 9 cm^{-1} to steel. The 3D structure of the samples was visualized by showing the two phases, crack and corrosion products, in the xy- and the yz-planes (Figure 5.12).

At time t_0, the low-carbon steel sample did not show any trace of corrosion products or cracks. At time t_1, corrosion products had already accumulated around the steel rebar. They also started to migrate outward, filling up the walls of an air void with a diameter of about 0.3 mm. Two thin radial cracks formed: crack #1 reached the external face of the cement paste, while crack #2 was still small. Between time t_1 and time t_2, more corrosion products accumulated around the steel bar, and some migrated out in the lower right direction, next to crack #1, but not following it. Crack #2 grew longer and reached the external face of the cement paste matrix. Between time t_2 and time t_3, more corrosion products accumulated around the steel bar, and continued to migrate next to crack #1. Furthermore other corrosion products started to migrate and deposit along crack #2.

At time t_3, a larger vertical portion of the sample was scanned (Figure 5.12). The rebar is shown from the tip of the steel rebar (top) down to next to the solder with the electrical wire (bottom). While the shapes of the radial cracks were homogeneous throughout the sample, the pattern of the migrating corrosion products was rather intricate. Going from the solder to the tip, gradually more corrosion products migrated away from the reinforcing bar, producing a non-uniform propagation front.

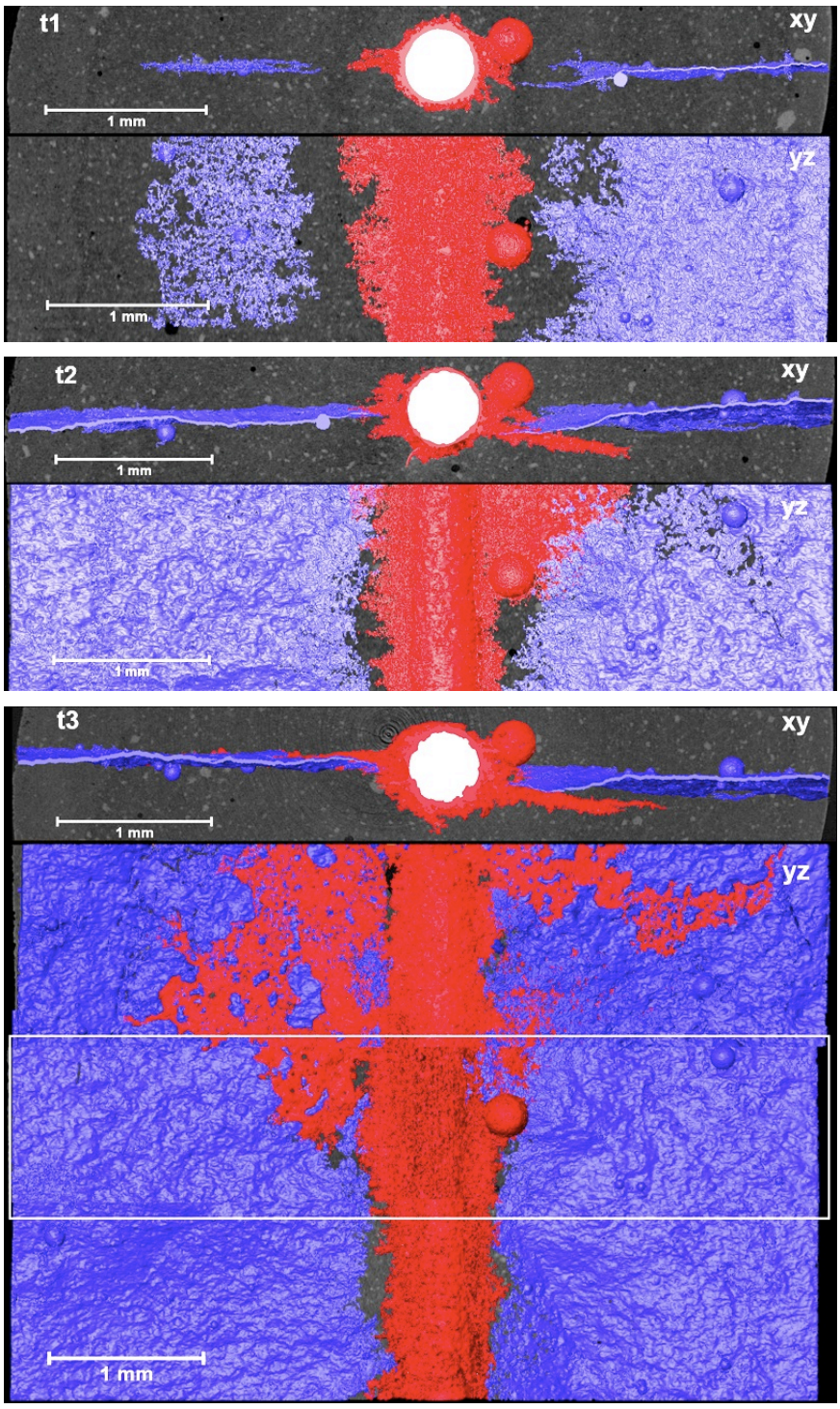

Figure 5.12 2-phase segmentation of the low-carbon steel sample at times t_1, t_2, and t_3. Corrosion products migrating outward (red), and crack propagating (blue). View in the xy-plane (top) and in the yz-plane (bottom). At time t_3, an extended portion of the rebar is displayed in the yz-plane: previous portion boxed in white.

5.2. Discussion

5.2.1. Corrosion mechanism

Passive state. A passive film naturally forms in alkaline environment such as the one found in ordinary portland cement concrete (see Chapter 3). During a first stage, this passive film protects the steel from corroding. During a galvanostatic reduction, the current density is held constant, hence the higher the resistance of this film, the higher the potential at the reinforcing bar.

During the initiation period, we observed that: E_G(low-carbon)< E_G(Top12)< E_G(LDX 2101) (Figure 5.1). This indicated that the resistance of the passive film created on LDX 2101 steel was higher that the resistance on Top12 steel, which was also higher than the resistance of low-carbon steel. According to the elemental composition (Table 1), LDX 2101 contained more chromium (17%) than Top12 (11%), and low-carbon steel contained no chromium. Steels with higher chromium content developed more protective passive films (see Chapter 4).

Passive film breakdown. After some time of applying a constant current density, the potential decreased, indicating that the passive film had broken down, and that active corrosion started.

For the low-carbon steel the potential suddenly dropped down of about 1V after 45min (Figure 5.1), while for the Top12 steel, the potential slowly decreased after 1 hour of galvanostatic corrosion. Finally for the LDX 2101 steel, we observed no potential decrease during the 3 hours it was galvanostatically tested.

The higher the chromium content the longer it took for the passive film to break down: the passive film formed on the LDX 2101 steel did not alter during the impression of the current. For the low-carbon steel, the break down was sudden: the whole bar depassivated at the same time. Conversely, for the Top12 steel, the passive film broke down gradually, with the resistance of the reinforcing bar (E_G/i_G) gradually decreasing.

Crack formation. Right after the potential decreased for the low-carbon steel and the Top12 steel, a radial crack initiated (Figure 5.2 and Figure 5.3).

Once the passive film broke down, active corrosion started and corrosion products formed at the surface of the steel. These products expanded, and generated stresses in the cement paste matrix. In particular, the hoop stress put the matrix in tension, with cement paste being a lot weaker in tension than in compression. The cement paste thus broke, and a radial crack propagated from the steel toward the exterior of the sample.

Corrosion product migration. In the low-carbon and the Top12 steel specimens, after cracks formed, corrosion products gradually deposited on the walls of the cracks (Figure 5.2 and Figure 5.3).

While the constant anodic current density formed corrosion products at the surface of the steel, it also generated an electric field acting on the positively charged iron oxides. They were pulled outward and eventually precipitated onto neutral insoluble products on the walls of the cracks, and in the air voids. When no external current is applied, diffusion can also cause the migration of the corrosion products, but at a slower

rate. For samples immersed in sea water, Zhao *et al.* observed the migration of the corrosion products through the open cracks (Zhao et al. 2012). They noticed that corrosion products start to leach out only when the crack has fully cracked the concrete cover. From the reconstructed tomograms in Figure 5.2, it seemed that at time t_2, the corrosion products leached out without any crack reaching the outer-part of the cement paste cover. However, from the 3D segmented image in Figure 5.11, it appeared that these corrosion products are at the bottom of a crack that was connected to a major crack that went through the whole cement paste cover. The corrosion products belong hence to an open crack network, in agreement with Zhao *et al.* This highlights the advantages of getting the full 3D structure of the crack system from µCT.

5.2.2. Localized versus generalized corrosion

The corrosion attack on the low-carbon steel was pervasive, i.e., the whole surface homogeneously corroded away (Figure 5.2). For the Top12 steel, localized pits were nucleating and growing, causing a heterogeneous corrosion of the surface. At the end of the experiment, only a quarter of the surface had been attacked by corrosion (Figure 5.3).

Once the passive film formed on low-carbon steel broke down, even if it was only on a small location, a microcell formed, and the rest of the passive film broke down as well. In the case of the Top12 steel, when a small area of the film depassivated, the rest of the passive film remained strong enough to hold and not corrode. It disabled the transition of metastable pitting into stable pit propagation (Moser et al. 2012). When the pit eventually transformed into a stable pit, only a small area corroded away. However small this area was, the steel cross-section is sensibly reduced; this can cause issues to the mechanical properties of the steel rebar.

This was consistent with the potential profile. The resistance of the reinforcing bar (E_G/i_G) depends on the resistance of all part of the passive film. If the whole surface depassivated at once, the resistance would suddenly drop, like it happened for the low-carbon steel (Figure 5.1). If only part of the film depassivated, then the resistance of the passivated area and the resistance of the depassivated area would create a parallel electric circuit. Henceforth, with a growing depassivated area, the conductance of the specimen increased, and the resistance decreased, just like it was seen for the Top12 steel specimen.

5.2.3. Average penetration

Faraday's equation provides a convenient way to predict the amounts of species that are produced/reacted during an electrochemical reaction, e.g. $A \rightarrow A^{n+} + n.e^{-}$:

$$m = ItM/nF$$

where m is the mass of oxidized metal, I is the current, t is the time, M is the molar mass of the metal, n is the number of exchanged electrons, and $F = 96{,}500\ C/mol$ is the Faraday's constant.

The average thickness loss, δ, is obtained by dividing m by the exposed surface of metal, and by its density, ρ:

$$\delta = itM/nF\rho$$

where $i = I/A$ is the current density. For iron, $n = 2$, $M = 55.9\ g/mol$, $\rho = 7.87\ g/cm^3$, hence:

$$\delta = 1.332it \quad (\mu m)$$

with i in mA/cm^2 and t in hours. This predictive formula is compared with the measured values from the µCT experiment (Figure 5.13).

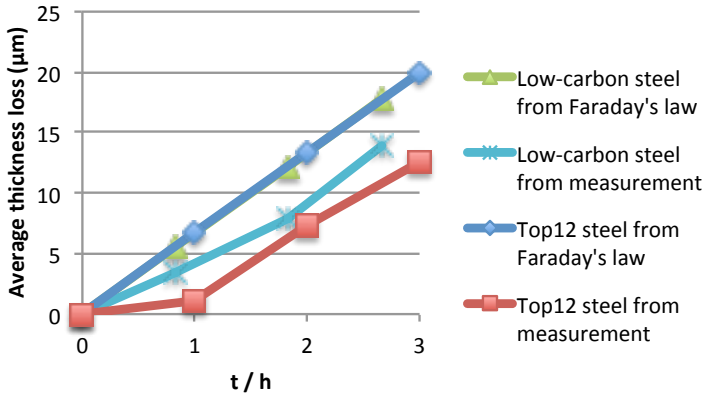

Figure 5.13 Comparison between the steel average thickness losses predicted by Faraday's law and measured by µCT for the low-carbon and the Top12 steel.

We observed that the volume loss predicted by the Faraday's equation was, for all cases, larger than the volume loss measured by the µCT experiments. This was particularly striking for the LDX 2101 steel, where no volume loss was observed even though a steady electron current flow of 5mA/cm^2 was impressed through the steel reinforcing bar. When steel is in a passive state, the film has a resistance R_P (related to E_G/i_G, see section 5.2.1). Since the passive film is a good electron conductor but an ionic insulator, no expansive iron oxides are formed while the steel is in a passive state.

After the initiation period, once the passive film has broken down, the average penetration grew linearly with time, at a rate close to the rate predicted by Faraday (**Figure 5.13**). Some corrosion mechanism models include nonlinear corrosion products growth (Bhargava et al. 2005). After corrosion products have formed, they influence the behavior of the steel; a layer of corrosion products blocks the continuous formation of new products. The effect of the accumulation of corrosion products on the corrosion product growth is described by nonlinear equations (Liu and Weyers 1998). However, no evidence of this behavior has been observed in this experiment. When reinforced cement paste is naturally corroding, the main migration force for the corrosion products is diffusion, whereas when it is galvanostatically corroded, such as in this study, the main

migration force is of electrostatic nature. The latter imposed an electrical field that attracted the charged soluble iron oxides away from the steel interface, lessening the amount of corrosion products accumulating at the surface of the reinforcing bar. Therefore the amount of corrosion was linearly growing, at the rate predicted by Faraday's law.

5.2.4. Corrosion products type

The linear attenuation coefficient, μ, is the average by mass of the mass attenuation coefficients $(\mu/p)_i$ with weight, f_i , of each atom, i, multiplied by the density, δ:

$$\mu = \delta \sum_i f_i \, (\mu/p)_i$$

At photon energy 47keV, the linear attenuation coefficient of steel is expected to be 18.3cm^{-1}, and the cement paste (calcium-silicate-hydrate phase) 1.4 cm^{-1}. These two values are close from the measured ones. For denser iron oxides, like iron(II)-oxide FeO, the linear attenuation coefficient is 10.6 cm^{-1}, and for less dense iron oxides, like iron hydroxides $Fe(OH)_2$ (resp. $Fe(OH)_3$), it is 5.2 cm^{-1} (resp. 4.5 cm^{-1}). For hydrated iron hydroxide $Fe(OH)_3.3H_2O$, the linear attenuation is lower, 3.4 cm^{-1}. This last value is greater than the 3.2 cm^{-1} measured in the sample (Figure 5.10), indicating a lower density for the corrosion products. From the segmented images, we also measured a volume of the corrosion products 8 times greater than the volume of lost steel for the Top12 steel sample at time t_3, whereas the specific volume for hydrated iron hydroxide is about 6.5 (Figure 1.4). This also indicated that the corrosion products were less dense/had high specific volume. The probing volume of the µCT instrument was 3.3µm x 3.3µm x 3.3µm: it was not able to distinguish microstructural features below this size. In particular, the corrosion products can form a porous network with pores below the micrometer scale; this may lower the measured density.

5.2.5. Mechanical model of the crack propagation in the sample

Knowing the mechanical properties of the matrix, it is possible to relate the hoop stress at the interface between the corrosion products and the cement paste matrix to the corrosion rate. Piltner and Monteiro introduced a factor p to take into account the volume gain by corrosion products for an infinite matrix (Piltner and Monteiro 2000). p is the ratio between the relative difference between the specific volumes of the corrosion products, ν_c, and steel, ν_s ($p = (\nu_c - \nu_s)/\nu_s$). In a cylindrical geometry with finite boundary conditions, Li and Weyers linked the amount of corrosion products formed to the tension in the concrete matrix, and developed a non-linear model for the time-to-cracking, and corrosion product formation (Liu and Weyers 1998).

The mechanical problem of two coaxial cylinders with radii a and A is solved in cylindrical coordinates considering the material as linear elastic (Figure 5.14). For geometries that are not exactly cylindrical, Liu and Weyers proposed to approximate it by a cylindrical geometries, by using a as the rebar radius, and where $A = C$ is the distance from the center to the cover (Liu and Weyers 1998).

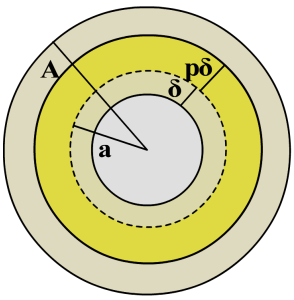

Figure 5.14 Schematic of a cylindrical steel rebar with radius *a* embedded in a cylindrical cement paste sample with radius *A*. The steel rebar is corroded by a thickness δ, and the corrosion products' expansion imposes a displacement $p\delta$ at the interface.

In plane stress with cylindrical coordinates, the equilibrium equation is

$$\frac{d\sigma_r}{dr} + \frac{\sigma_r - \sigma_\theta}{r} = 0$$

where σ is the stress and indices r stand for radial, and θ for orthoradial. Strain-displacements relationships in cylindrical coordinates are

$$\epsilon_r = \frac{du}{dr};\ \epsilon_\theta = \frac{u}{r}$$

where u is the radial displacement and ϵ is the strain. Assuming that the matrix behaves in an isotropic linear elastic behavior, the stresses σ write

$$\sigma_r = \frac{E}{1-\nu^2}(\epsilon_r + \nu\epsilon_\theta);\ \sigma_\theta = \frac{E}{1-\nu^2}(\epsilon_\theta + \nu\epsilon_r)$$

where E is the modulus of Elasticity for the matrix and ν is the Poisson's ratio. Solving the linear elastic problem gives

$$\begin{cases} u = \dfrac{\alpha r}{2} + \dfrac{\beta}{r} \\ \sigma_r = \dfrac{E}{1-\nu^2}\left(\dfrac{\alpha}{2}(1+\nu) - \dfrac{\beta}{r^2}(1-\nu)\right) \\ \sigma_\theta = \dfrac{E}{1-\nu^2}\left(\dfrac{\alpha}{2}(1+\nu) + \dfrac{\beta}{r^2}(1-\nu)\right) \end{cases}$$

where α and β are two constants determined by the boundary conditions. In this case, the radial stress on the outer-part of the matrix is zero: $\sigma_r(A) = 0$. When a thickness δ of the steel rebar is corroded away, it imposed a displacement $p\delta$ at the interface between the two materials: $u(a) = p\delta$ (Figure 5.14). Solving the linear system of equation for α and β, with $x = A/a$ the aspect ratio, it becomes

$$\begin{cases} u = \dfrac{p\delta}{1-\nu+x^2(1+\nu)}\left((1-\nu)\dfrac{r}{a}+x^2(1+\nu)\dfrac{a}{r}\right) \\ \sigma_r = \dfrac{Ep\delta/a}{1-\nu+x^2(1+\nu)}\left(1-\dfrac{A^2}{r^2}\right) \\ \sigma_\theta = \dfrac{Ep\delta/a}{1-\nu+x^2(1+\nu)}\left(1+\dfrac{A^2}{r^2}\right) \end{cases}$$

When corrosion products start building up at the interface, the pressure is positive (i.e., $p\delta > 0$). Therefore the hoop stress, σ_θ, is in tension, and it is maximal at the interface (i.e., for $r = a$). The critical hoop stress, σ_C, when the concrete starts to crack, is $\sigma_C = \sigma_\theta(a) = f_t'$ and therefore

$$p\delta_C = \frac{af_t'}{E}\left(1+\nu\frac{x^2-1}{x^2+1}\right)$$

Samples in this study have a 0.5 mm-diameter steel reinforcing bar, in a 5 mm-diameter cement paste matrix, therefore $x = 10$ and $x^2 \gg 1$.

$$p\delta_C = \frac{af_t'}{E}(1+\nu)$$

Cracks initiate at the surface of the steel, and then propagate outward to finally reach the outer-surface of the matrix. Molina *et al.* proposed a model to take into account the widening of the crack as the corrosion products accumulate at the steel/concrete interface (Molina, Alonso, and Andrade 1993). Assuming than once cracked, the concrete is free of stresses and moves in a rigid motion, the width of the crack is constant throughout its all length, and the sum of all crack widths, Σw_i, is $2\pi p\delta$. From Figure 5.5, it seems that next to the steel/cement paste interface, the crack widened linearly with distance to the interface, and then, away from the interface, the crack width become uniform. This crack shape can also be seen in the xy-plane views, Figure 5.12. In the region close to the interface, it is contradicting the crack shape with uniform width proposed by Molina *et al.* However focusing on this region for the low-carbon steel sample in the reconstructed tomograms of Figure 5.2, many thin cracks can be seen, with widths at the limit of the instrument's resolution (voxel size is 3.3x3.3x3.3 μm^3), and thinner cracks could not be observed. It is therefore possible that the sum of all these crack widths is constant for all distances, which would be in agreement with Molina *et al.*'s model. The voxel size however prevents from taking into account the ensemble of the cracks in the region close to the steel interface.

Furthemore, Zhao *et al.* described a mechanism of crack formation in 3 steps (Zhao et al. 2012). First the crack initiates, and grows radially outward. Second, once it has fully cracked the concrete cover, the outer solution can directly reach the steel/cement paste interface and corrosion forms at the tip of the crack. Third, the accumulation of corrosion products at the tip of the crack causes stresses that open the crack linearly with the distance to the center. A corollary of this mechanism is that corrosion products can only migrate out through an open crack. In agreement with the observation by Zhao *et al.*, it is seen for Top12 steel in the reconstructed tomograms of Figure 5.3, that no corrosion

products migrated out of the crack that did not reach the surface of the cement paste cover (third crack, opposite to the 2 main ones). Furthermore, on the low-carbon steel sample in Figure 5.2, it appears that corrosion products are migrating out of a crack that is not reaching the concrete cover. But from the segmentation of the full height sample in Figure 5.12, the crack is actually belonging to a crack network that contains an open crack, which is in agreement with Zhao *et al.*

5.3. Summary

The corrosion of steel embedded in cement paste is accelerated by applying a galvanostatic anodic current density of 5 mA/cm^2 for 3 hours, and the corrosion mechanism of steel embedded in cement paste is monitored by micro-computed tomography (μCT) in a non-destructive manner. First, the passive film formed on steel delays the onset of corrosion. After this initiation period, the passive film breaks down and corrosion products starts to accumulate at the interface between the steel and the cement paste. When the corrosion products' pressure reaches the tensile strength of the cement paste, cracks initiate at the steel interface and radially propagate toward the outer part of the cement paste. Finally, the corrosion products migrate through the cracks and deposit on their walls.

Three grades of steel show different corrosion behaviors. A sudden drop of the low-carbon steel potential difference is associated with a generalized breakdown of its passive film, and a subsequent homogeneous corrosion of its surface. The Top12 ferritic stainless steel the potential difference decreases gradually, in association with a partial breakdown of the passive film, and the formation of localized corrosion pits. Upon comparable amounts of exchanged charges, no corrosion is observed on the LDX 2101 duplex stainless steel.

μCT gives quantitative information about the microstructural changes of steel corroding in cement paste. A comparison between the volume loss measured by μCT and the predicted values from Faraday's law confirms the accuracy of the latter. Furthermore, the crack width evolution with distance from the center is constant in the outer-part of the surrounding cement paste, and a more complex crack network formed in the region close to the steel interface. Finally, the corrosion products have a linear attenuation coefficient lower than the values expected for iron and chromium oxides, maybe underestimating the porosity of the corrosion products at the sub-micron scale.

Most strikingly, galvanostatic corrosion creates deep corrosion pits at the surface of Top12 ferritic stainless steel. These pits form localized corrosion products that induce stress concentrations at the steel/concrete interface. This has a very negative influence on the dynamic of the cracks forming in the structure, and can put the whole reinforced concrete structure at risk. To confirm this behavior, it is necessary to carry complementary studies. First, the experiment should be reproduced with lower galvanostatic current densities. Second, the corrosion of Top12 ferritic stainless steel could be induced without the application of an external current, in more "natural" ways, like by immersing the sample in a chloride solution, or by carbonating the cement paste in order to facilitate the early breakdown of the steel's passive film.

Chapter 6: Conclusion

The corrosion performances of low-carbon and stainless steels have been investigated at both the nanometer-scale and the micrometer-scale using powerful non-destructive techniques. First, synchrotron-based x-ray photoelectron spectroscopy (XPS) has shown to be the adequate tool to observe few-nanometer-thick passive layers. The passive state of the steels in alkaline environments dictates the corrosion initiation, a period when steel is protected from the harmful effects of corrosion. Then, micro-computed tomography (μCT) has allowed monitoring the *in-situ* evolution of corrosion in reinforced concrete samples. Active corrosion of steel embedded in concrete dictates the extent of the damages to the structure.

Chapter 3 indicates that monitoring the polarization resistance of naturally growing films, along with cyclically polarizing the low-carbon steel (ASTM A36) electrode, provides useful information about the kinetics of the passive film formation. A synchrotron-based XPS method provides additional insight in the oxide composition, the layered structure and the stability of the passive film formed on low-carbon steel over a wide range of highly alkaline solutions. They correspond to environments found in ordinary portland cement concretes as well as in inorganic polymer concretes made by alkali-activating fly ash type F, type C, and ground granulated blast-furnace slag. These data are critical in understanding how the high pH of the pore fluids found in environmentally friendly inorganic polymer concretes influence the stability of the passive film protecting the steel reinforcements. The experimental investigations demonstrate that most of the films appear to have reached the passivation stage after 30-minute immersion. XPS measurements on the Fe3p peak reveal that higher alkali content caused a decrease in the thickness of the oxide film. Non-invasive XPS depth profiling captured the thickening of a passive film formed in the 0.1 M solution, from 2.4 nm at 30 min to 4.1 nm after 2 days of immersion. This was accompanied by an enrichment of its outermost layer in iron(III)-oxide. This is a key factor in the increase in polarization resistance of the passive film over time. Corrosion current densities increase with solution alkalinity, indicating a less protective films at high pH. In addition, the formation of soluble iron(II)-oxides at low potentials in highly alkaline environments may cause the formation of a less protective oxide layer in the early age of the passive film.

In chapter 4, a similar experimental procedure has been carried for LDX 2101 duplex stainless steel (UNS S32101) immersed in the same alkaline solutions. In addition, the Cr3p XPS peak was also measured to evaluate the importance of chromium oxide in the passive oxide layer. Changing the incident photon energy from low to high, the passive film is probed at different depths, and layering models can quantify the enrichment of the film in chromium oxide. The experimental results show that similarly to low-carbon steel, the iron oxide film formed on LDX 2101 stainless steel grows thinner and poorer in iron(III)-oxide as the alkalinity of the solution increases. However the passive film is enriched in chromium(III)-oxide at increasing alkalinities. This enrichment stabilizes the corrosion performances for higher alkalinities. The XPS depth profile shows that after 2 days, the film grown in the 0.1 M solution is 2.8-nm thick and contains some chromium(III)-oxide in its outer-layer.

Chapter 5 provides qualitative as well as quantitative information about the propagation of corrosion for steel embedded in cement paste. Applying an external anodic current of 5 mA/cm^2 accelerate corrosion in a reproducible manner on low-carbon steel (ASTM A36), Top12 ferritic stainless steel (UNS S41000), and LDX 2101 duplex stainless steel (UNS S32101). The crack patterns and the propagation of the corrosion products are observed non-invasively by μCT, allowing analyzing the mechanisms in a time-resolved manner. Quantitative measurements of the linear attenuation coefficients and the size of the features are also performed. The experimental results resolve the cracked cement paste, the propagating corrosion products, and the corroded steel with a resolution of few micrometers. The corrosion-induced cracks form radially, and widen with the accumulation of corrosion products at the steel/concrete interface. Once the passive film breaks down, the average steel loss measured by μCT and predicted by Faraday's law correlate well. A major difference between the low-carbon steel and Top12 stainless steel lies in their corrosion mechanism. Low-carbon steel shows a homogeneous corrosion, with the entire surface gradually etched away, while Top12 stainless steel corrodes locally, with the formation of corrosion pits distributed over a quarter of its surface. No sign of corrosion is observed on LDX 2101 duplex stainless steel.

The protective character of the passive film forming on low-carbon steel is optimal in the alkalinity range of 0.1 M to 0.6 M, corresponding to pH from 13 to 13.8. This range corresponds to the alkalinity found in the pores of ordinary portland cement concrete, in which real-time exposures have proven to provide good resistance to the initiation of corrosion on low-carbon steel reinforcing bars. Unfortunately, solutions with higher alkalinity induce significant decrease in the corrosion resistance of the film, and in concretes where the pore solution alkalinity is expected to be high, such as non-carbonated IPC, the corrosion resistance during the initiation period is expected to be substantially lower than that of conventional OPC concretes. Conversely, duplex stainless steel performs well with respect to corrosion in the whole range of alkalinity, and it can be considered as reinforcement for concretes with highly alkaline pore solutions. Past this initiation period, the mechanism of active corrosion for the selected steel must also be examined to draw the complete picture of its corrosion resistance in reinforced concrete structures. While low-carbon steel corrodes homogeneously, ferritic stainless steel corrodes locally, concentrating the corrosion-induced stresses, and causing higher damage to the structure. Hence, there are disadvantages in using some grades of stainless steels in harsh environments.

References

A276. 2012. “Standard Specification for Stainless Steel Bars and Shapes.” *ASTM International* 10: 1–7.

ACI Committee E-701, Materials for Concrete Construction. 2006. “REINFORCEMENT FOR CONCRETE — MATERIALS AND APPLICATIONS.” *ACI Education Bulletin E2-00*: 1–16.

Abreu, C. M., M.J. Cristóbal, and R. Losada. 2004. “Comparative Study of Passive Films of Different Stainless Steels Developed on Alkaline Medium.” *Electrochimica Acta* 49: 3049–3056.

Addari, D., B. Elsener, and A. Rossi. 2008. “Electrochemistry and Surface Chemistry of Stainless Steels in Alkaline Media Simulating Concrete Pore Solutions.” *Electrochimica Acta* 53 (27): 8078–8086.

Allen, G.C., P.M. Tucker, and R.K. Wild. 1978. “X-ray Photoelectron/Auger Electron Spectroscopic Study of the Initial Oxidation of Chromium Metal.” *J. Chem. Soc., Faraday Trans. 2* (X): 1126–1140.

Andrade, C., C. Alonso, and F.J. Molina. 1993. “Cover Cracking as a Function of Bar Corrosion: Part 1-Experimental Test.” *Materials and Structures* 26: 453–464.

Andrade, C., and J.A. González. 1978. “Quantitative Measurements of Corrosion Rate of Reinforcing Steels Embedded in Concrete Using Polarization Resistance Measurements.” *Werkstoffe Und Korrosion* 29 (8): 515–519.

Bautista, A., G. Blanco, F. Velasco, A. Gutiérrez, L. Soriano, F.J. Palomares, and H. Takenouti. 2009. “Changes in the Passive Layer of Corrugated Austenitic Stainless Steel of Low Nickel Content Due to Exposure to Simulated Pore Solutions.” *Corrosion Science* 51 (4): 785–792.

Bentur, A., S. Diamond, and N.S. Berke. 1997. *Steel Corrosion in Concrete: Fundamentals and Civil Engineering Practice*. London; New York: E & FN Spon.

Berke, N.S., and T.G. Weil. 1992. “World Wide Review of Corrosion Inhibitors in Concrete.” *Advances in Concrete Technology*: 899–924.

Bertolini, L., F. Bolzoni, T. Pastore, and P. Pedeferri. 1996. “Behaviour of Stainless Steel in Simulated Concrete Pore Solution.” *British Corrosion Journal* 31 (3): 218–222.

Beverskog, B., and I. Puigdomenech. 1996. “Revised Pourbaix Diagrams for Iron at 25-300 ° C.” *Corrosion Science* 38 (12): 2121–2135.

Bhargava, K., A. K. Ghosh, Y. Mori, and S. Ramanujam. 2005. “Modeling of Time to Corrosion-induced Cover Cracking in Reinforced Concrete Structures.” *Cement and Concrete Research* 35: 2203–2218.

Bockris, J.O’M., A. K.N. Reddy, and M. Gamboa-Aldeco. 2000. *Modern Electrochemistry 2A*. 2nd edition. New York: Kluwer Academic / Plenum Publishers.

Brion, D. 1980. “Etude Par Spectroscopie De Photoelectrons De La Degradation Superficielle De FeS2, CuFeS2, ZnS Et PbS a L’air Et Dans L'eau.” *Applications of Surface Science* 5: 133–152.

Broomsfield, J.P. 1997. *Corrosion of Steel in Concrete: Understanding, Invastigationm and Repair*. London; New York: E & FN Spon.

Büchler, M., P. Schmuki, and H. Böhni. 1997. “Formation and Dissolution of the Passive Film on Iron Studied by a Light Reflectance Technique.” *Journal of the Electrochemical Society* 144 (7): 2307–2312.

Callaghan, B.G. 1993. “The Performance of a 12% Chromium Steel in Concrete in Severe Marine Environments.” *Corrosion Science* 35 (5-8): 1535–1541.

Carino, N.J. 1999. “Nondestructive Techniques to Investigate Corrosion Status in Concrete Structures.” *Journal of Performance of Constructed Facilities* 13 (3): 96–106.

Caré, S., Q.T. Nguyen, V. L’Hostis, and Y. Berthaud. 2008. “Mechanical Properties of the Rust Layer Induced by Impressed Current Method in Reinforced Mortar.” *Cement and Concrete Research* 38 (8-9): 1079–1091.

Concrete Reinforcing Steel Institute. 2008. *Building Green with Reinforced Concrete*.

Cornell, R.M., and U. Schwertmann. 2003. *The Iron Oxides : Structure, Properties, Reactions, Occurrences, and Uses*. Second edition. Wiley-VCH.

Criado, M., D.M. Bastidas, S. Fajardo, A. Fernández-Jiménez, and J.M. Bastidas. 2011. “Corrosion Behaviour of a New Low-nickel Stainless Steel Embedded in Activated Fly Ash Mortars.” *Cement and Concrete Composites* 33 (6): 644–652.

Descostes, M., F. Mercier, N. Thromat, C. Beaucaire, and M. Gautier-Soyer. 2000. “Use of XPS in the Determination of Chemical Environment and Oxidation State of Iron and Sulfur Samples: Constitution of a Data Basis in Binding Energies for Fe and S Reference Compounds and Applications to the Evidence of Surface Species of an Oxidized Py.” *Applied Surface Science* 165 (4): 288–302.

Deventer, J.S.J., J. L. Provis, P. Duxson, and D.G. Brice. 2010. "Chemical Research and Climate Change as Drivers in the Commercial Adoption of Alkali Activated Materials." *Waste and Biomass Valorization* 1 (1): 145–155.

Duxson, P., A. Fernández-Jiménez, J.L. Provis, G.C. Lukey, A. Palomo, and J.S.J. Deventer. 2007. "Geopolymer Technology: The Current State of the Art." *Journal of Materials Science* 42: 2917–2933.

Elsener, B., D. Addari, S. Coray, and A. Rossi. 2011. "Nickel-free Manganese Bearing Stainless Steel in Alkaline media—Electrochemistry and Surface Chemistry." *Electrochimica Acta* 56 (12): 4489–4497.

Fairley, N. "CasaXPS VAMAS Processing Software." http://www.casaxps.com/.

Federal Highway Administration. 2002. "Corrosion Cost and Preventive Strategies in the United States." *NACE International* FHWA-RD-01.

Fernández-Jiménez, A., and A. Palomo. 2007. "Factors Affecting Early Compressive Strength of Alkali Activated Fly Ash (OPC-free) Concrete." *Materiales De Construcción* 57: 7–22.

Fernández-Jiménez, A., A. Palomo, and C. López-hombrados. 2006. "Engineering Properties of Alkali-Activated Fly Ash Concrete." *ACI Materials Journal* (March-April): 106–112.

Freire, L., X.R. Nóvoa, M.F. Montemor, and M.J. Carmezim. 2009. "Study of Passive Films Formed on Mild Steel in Alkaline Media by the Application of Anodic Potentials." *Materials Chemistry and Physics* 114 (2-3): 962–972.

Gallucci, E., K. Scrivener, A. Groso, M. Stampanoni, and G. Margaritondo. 2007. "3D Experimental Investigation of the Microstructure of Cement Pastes Using Synchrotron X-ray Microtomography (μCT)." *Cement and Concrete Research* 37: 360 – 368.

García-Alonso, M.C., M.L. Escudero, J.M. Miranda, M.I. Vega, F. Capilla, M.J. Correia, M. Salta, A. Bennani, and J.A. González. 2007. "Corrosion Behaviour of New Stainless Steels Reinforcing Bars Embedded in Concrete." *Cement and Concrete Research* 37 (10): 1463–1471.

Gartner, E. 2004. "Industrially Interesting Approaches to 'low-CO2' Cements." *Cement and Concrete Research* 34 (9): 1489–1498.

Ghahari, S.M., A.J. Davenport, T. Rayment, T. Suter, J.-P. Tinnes, C. Padovani, J.A. Hammons, M. Stampanoni, F. Marone, and R. Mokso. 2011. "In Situ Synchrotron X-ray Micro-tomography Study of Pitting Corrosion in Stainless Steel." *Corrosion Science* 53 (9): 2684–2687.

Ghods, P., O.B. Isgor, J.R. Brown, F. Bensebaa, and D. Kingston. 2011. "XPS Depth Profiling Study on the Passive Oxide Film of Carbon Steel in Saturated Calcium Hydroxide Solution and the Effect of Chloride on the Film Properties." *Applied Surface Science* 257 (10): 4669–4677.

Ghods, P., O.B. Isgor, G. McRae, and T. Miller. 2009. "The Effect of Concrete Pore Solution Composition on the Quality of Passive Oxide Films on Black Steel Reinforcement." *Cement and Concrete Composites* 31 (1): 2–11.

González, J.A., C. Andrade, C. Alonso, and S. Feliu. 1995. "Comparison of Rates of General Corrosion and Maximum Penetration on Concrete Embedded Steel Reinforcement." *Cement and Concrete Research* 25 (2): 257–264.

Grass, M.E., P.G. Karlsson, F. Aksoy, M. Lundqvist, B. Wannberg, B.S. Mun, Z. Hussain, and Z. Liu. 2010. "New Ambient Pressure Photoemission Endstation at Advanced Light Source Beamline 9.3.2." *The Review of Scientific Instruments* 81 (053106).

Gries, W.H. 1996. "A Universal Predictive Equation for the Inelastic Mean Free Pathlengths of X-ray Photoelectrons and Auger Electrons." *Surface and Interface Analysis* 24: 38–50.

Habert, G., J.-B. d' Espinose de Lacaillerie, and N. Roussel. 2011. "An Environmental Evaluation of Geopolymer Based Concrete Production: Reviewing Current Research Trends." *Journal of Cleaner Production* 19 (11): 1229–1238.

Haupt, S., and H.-H. Strehblow. 1987. "Corrosion, Layer Formation, and Oxide Reduction of Passive Iron in Alkaline Solution: a Combined Electrochemical and Surface Analytical Study." *Langmuir* 3 (6): 873–885.

Haupt, S., and H.-H. Strehblow. 1989. "Combined Electrochemical and Surface Analytical Investigations of the Formation of Passive Layers." *Corrosion Science* 29 (2/3): 163–182.

Hime, W.G. 1993. "Corrosion of Steel-Random Thoughts and Wishful Thinking." *Concrete International* 15 (10): 54–57.

Jin, S., and A. Atrens. 1987. "ESCA-Studies of the Structure and Composition of the Passive Film Formed on Stainless Steels by Various Immersion Times." *Applied Physics A* 42: 149–165.

Joiret, S., M. Keddam, C. Rangel, and H. Takenouti. 2002. "Use of EIS, Ring-disk Electrode, EQCM and Raman Spectroscopy to Study the Film of Oxides Formed on Iron in 1 M NaOH." *Cement and Concrete Composites* 24: 7–15.

Kak, A.C., and M. Slaney. 1999. *Principles of Computerized Tomogrpahic Imaging*. Ed. The institute of Electrical and Electronics Engineers Inc. New York: IEEE Press.

Liu, Y., and R.E. Weyers. 1998. "Modeling the Time-to-Corrosion Cracking in Chloride Contaminated Reinforced Concrete Structures." *ACI Materials Journal* 95 (6): 675–681.

Lloyd, R.R., J.L. Provis, and J.S.J. Deventer. 2010. "Pore Solution Composition and Alkali Diffusion in Inorganic Polymer Cement." *Cement and Concrete Research* 40 (9): 1386–1392.

MacDonald, D.D., and B. Roberts. 1978. "The Cyclic Voltammetry of Carbon Steel in Concentrated Sodium Hydroxide Solution." *Electrochimica Acta* 23: 781–786.

Mancio, M. 2008. Dissertation: "Electrochemical and In-situ Surface-Enhanced Raman Spectroscopy (SERS) Study of Passive Films Formed on Low-Carbon Steel in Highly Alkaline Environments." University of California, Berkeley.

Manning, D.G. 1996. "Corrosion Performance of Epoxy-coated Reinforcing Steel: North American Experience." *Construction and Building Materials* 10 (5): 349–365.

Mehta, P.K. 2001. "Reducing the Environmental Impact of Concrete." *Concrete International*: 61–66.

Mehta, P.K., and B.C. Gerwick Jr. 1982. "Cracking-corrosion Interaction in Concrete Exposed to Marine Environment." *Concrete International* 4: 45–51.

Mehta, P.K., and P.J.M Monteiro. 2006. *Concrete: Microstructure, Properties, and Materials*. Third edition. McGraw-Hill.

Michel, A., B.J. Pease, M.R. Geiker, H. Stang, and J. Forbes. 2011. "Cement and Concrete Research Monitoring Reinforcement Corrosion and Corrosion-induced Cracking Using Non-destructive X-ray Attenuation Measurements." *Cement and Concrete Research* 41 (11): 1085–1094.

Miranda, J.M., A. Fernández-Jiménez, J.A. González, and A. Palomo. 2005. "Corrosion Resistance in Activated Fly Ash Mortars." *Cement and Concrete Research* 35 (6): 1210–1217.

Molina, F.J., C. Alonso, and C. Andrade. 1993. "Cover Cracking as a Function of Rebar Corrosion: Part 2-Numerical Model." *Materials and Structures* 26: 532–548.

Montemor, M.F., A.M.P. Simoes, and M.G.S. Ferreira. 1998. "Analytical Characterization of the Passive Film Formed on Steel in Solutions Simulating the Concrete Interstitial ELectrolyte." *Corrosion* 54 (5).

Moser, R.D., P.M. Singh, L.F. Kahn, and K.E. Kurtis. 2012. "Chloride-induced Corrosion Resistance of High-strength Stainless Steels in Simulated Alkaline and Carbonated Concrete Pore Solutions." *Corrosion Science* 57: 241–253.

Nagayama, M., and M. Cohen. 1962. "The Anodic Oxidation of Iron in a Neutral Solution." *Journal of the Electrochemical Society* 109 (9): 781–790.

Patnaik, P. 2003. *Handbook of Inorganic Chemicals*. McGraw-Hill.

Piltner, R., and P.J.M. Monteiro. 2000. "Stress Analysis of Expansive Reactions in Concrete." *Cement and Concrete Research* 30 (6) (June): 843–848.

Pourbaix, M. 1974. *Atlas of Electrochemical Equilibria in Aqueous Solutions*. Ed. Cebelcor. NACE Inter.

Rosenberg, A., C.M. Hansson, and C. Andrade. 1989. "Mechanisms of Corrosion of Steel in Concrete." In *Materials Science of Concrete*, 1:285–313.

Schmutz, P., and D. Landolt. 1999. "In-situ Microgravimetric Studies of Passive Alloys: Potential Sweep and Potential Step Experiments with Fe-25Cr and Fe-17Cr-33Mo in Acid and Alkaline Solution." *Corrosion Science* 41: 2143–2163.

Schroeder, V., and T.M. Devine. 1999. "Surface Enhanced Raman Spectroscopy Study of the Galvanostatic Reduction of the Passive Film on Iron" 146 (11): 4061–4070.

Scrivener, K.L. 2004. "Backscattered Electron Imaging of Cementitious Microstructures: Understanding and Quantification." *Cement and Concrete Composites* 26 (8): 935–945.

Shalon, R., and M. Raphael. 1959. "Influence of Sea Water on Corrosion of Reinforcement." *Journal of the American Concrete Institute* (55-76): 1251–1268.

Shodja, H.M., K. Kiani, and A. Hashemian. 2010. "A Model for the Evolution of Concrete Deterioration Due to Reinforcement Corrosion." *Mathematical and Computer Modelling* 52 (9-10): 1403–1422.

Shuttleworth, D. 1980. "Preparation of Metal-Polymer Dispersions by Plasma Techniques. An ESCA Investigation." *J. Phys. Chem.* 84: 1629–1634.

Strohmeier, B.R. 1990. "An ESCA Method for Determining the Oxide Thickness on Aluminum Alloys." *Surface and Interface Analysis* 15: 51–56.

Sánchez, M., J. Gregori, C. Alonso, J.J. García-Jareño, H. Takenouti, and F. Vicente. 2007. "Electrochemical Impedance Spectroscopy for Studying Passive Layers on Steel Rebars Immersed in Alkaline Solutions Simulating Concrete Pores." *Electrochimica Acta* 52 (27): 7634–7641.

Sánchez-Moreno, M., H. Takenouti, J.J. García-Jareño, F. Vicente, and C. Alonso. 2009. "A Theoretical Approach of Impedance Spectroscopy During the Passivation of Steel in Alkaline Media." *Electrochimica Acta* 54 (28): 7222–7226.

Taylor, H.F.W. 1997. *Cement Chemistry*. London: T. Telford.

Thompson, W.T., M.H. Kaye, C.W. Bale, and A.D. Pelton. 2000. "Pourbaix Diagrams for Multielement Systems." In *Uhlig's Corrosion Handbook*, ed. R Winston Revie, 125–136. Second edi. John Wiley & Sons, Inc.

Tuutti, K. 1980. "Service Life of Structures with Regard to Corrosion of Embedded Steel." *Special Publication* 65: 223–236.

Vlassenbroeck, J., B. Masschaele, V. Cnudde, M. Dierick, K. Pieters, L. Van Hoorebeke, and P. Jacobs. 2010. "Octopus 8: A High Performance Tomographic Reconstruction Package for X-ray Tube and Synchrotron micro-CT." In *Advances in X-ray Tomography for Geomaterials*, 167–173. ISTE.

World Business Council for Sustainable Development. 2009. *The Cement Sustainability Initiative, Cement Industry Energy and CO2 Performance: "Getting the Numbers Right."* Ed. World Business Council for Sustainable Development. Wahington DC.

Yeh, J.J., and I. Lindau. 1985. "Atomic Subshell Photoionization Cross Scetions and Asymmetry Parameters." *Atomic Data and Nuclear Data Tables* 32 (l-155).

Zhao, Y., J. Yu, B. Hu, and W. Jin. 2012. "Crack Shape and Rust Distribution in Corrosion-induced Cracking Concrete." *Corrosion Science* 55: 385–393.

Appendix

Table A.1 Densities and specific volumes of the main iron/chromium oxides

Compound	**Fe**	**Fe_3O_4**	**Fe_2O_3**	**FeOOH**	**$Fe(OH)_2$**
Name	Iron	Magnetite	Hematite	Iron oxy-hydroxide	Iron(II)-hydroxide
Density δ / g.cm^{-3} [a]	7.873	5.17	5.25	3.52	3.4
Molar mass M / g.mol^{-1}	55.85	231.55	159.70	88.86	88.87
Specific volume / cm^3.mol^{-1}	7.09	14.93	15.21	25.24	26.43

Compound	**$Fe(OH)_3$**	**$Fe(OH)_3.3H_2O$**	**Cr**	**Cr_2O_3**
Name	Iron(III)-hydroxide	Hydrated iron(III)-hydroxide	Chromium	Chromium(III)-oxide
Density δ / g.cm^{-3} [a]	3.4	3.5	7.15	5.22
Molar mass M / g.mol^{-1}	106.87	160.91	52.00	151.99
Specific volume / cm^3.mol^{-1}	31.43	45.98	7.27	29.12

[a] (Patnaik 2003)

Table A.2 Inelastic mean free paths (IMFP) and photoionization cross-section of iron/chromium oxides at photon energies 300 eV, 500 eV, and 700 eV.

Compound	**Fe**	**Fe_3O_4**	**Fe_2O_3**	**Cr**	**Cr_2O_3**
Name	Iron	Magnetite	Hematite	Chromium	Chromium(III)-oxide
IMFP at 300 eV / nm[a]	0.626	0.719	0.697	0.684	0.697
Cross-section at 300 eV / Mb[b]	0.6	-	-	0.5	-
IMFP at 500 eV / nm[a]	0.916	1.055	1.022	0.997	1.016
Cross-section at 500 eV / Mb[b]	0.25	-	-	0.2	-
IMFP at 700 eV / nm[a]	1.189	1.366	1.324	1.142	1.306
Cross-section at 700 eV / Mb[b]	0.13	-	-	0.1	-

[a] Inelastic mean free path (IMFP) computed from predictive formulae by Gries (Gries 1996)

[b] Photoionization cross-sections (Yeh and Lindau 1985)